

PipeMFL-240K: A Large-scale Dataset and Benchmark for Object Detection in Pipeline Magnetic Flux Leakage Imaging

Tianyi Qu*

qutianyi@hb-sais.com

SINOMACH Sensing Tech Co., Ltd
Shenyang, Liaoning, China

Huadong Song

songhuadong@hb-sais.com

SINOMACH Sensing Tech Co., Ltd
Shenyang, Liaoning, China

Guanlin Liu

liuguanlin@hb-sais.com

SINOMACH Sensing Tech Co., Ltd
Shenyang, Liaoning, China

Songxiao Yang*

syang@ok.sc.e.titech.ac.jp

Institute of Science Tokyo
Tokyo, Japan

Xiaoting Guo

guoxiaoting@hb-sais.com

SINOMACH Sensing Tech Co., Ltd
Shenyang, Liaoning, China

Haolin Wang*

haolin.wang.k3@elms.hokudai.ac.jp

Hokkaido University
Sapporo, Hokkaido, Japan

Wenguang Hu

huwenguang@hb-sais.com

SINOMACH Sensing Tech Co., Ltd
Shenyang, Liaoning, China

Yafei Ou†

yafei@ist.hokudai.ac.jp

Hokkaido University
Sapporo, Hokkaido, Japan

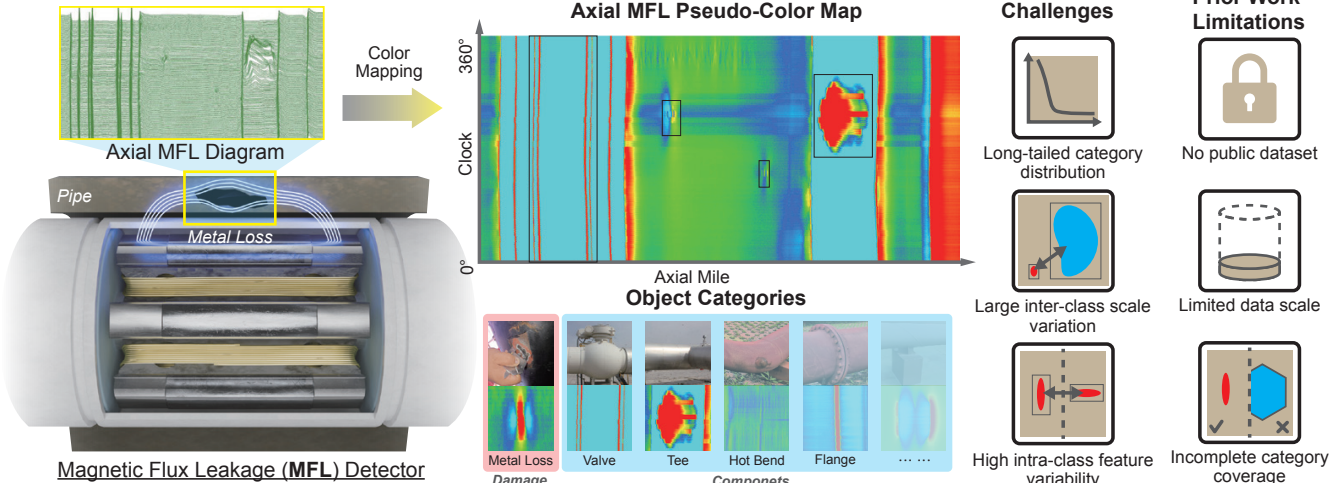


Figure 1: An overview of MFL detection, the key challenges it poses and the limitations of prior work.

Abstract

Pipeline integrity is critical to industrial safety and environmental protection, with Magnetic Flux Leakage (MFL) detection being a primary non-destructive testing technology. Despite the promise of deep learning for automating MFL interpretation, progress toward reliable models has been constrained by the absence of a large-scale public dataset and benchmark, making fair comparison and reproducible evaluation difficult. We introduce **PipeMFL-240K**, a large-scale, meticulously annotated dataset and benchmark for complex object detection in pipeline MFL pseudo-color images. PipeMFL-240K reflects real-world inspection complexity and poses several unique challenges: (i) an extremely long-tailed distribution over 12 categories, (ii) a high prevalence of tiny objects that often comprise

only a handful of pixels, and (iii) substantial intra-class variability. The dataset contains **240,320** images and **191,530** high-quality bounding-box annotations, collected from 11 pipelines spanning approximately **1,480** km. Extensive experiments are conducted with state-of-the-art object detectors to establish baselines. Results show that modern detectors still struggle with the intrinsic properties of MFL data, highlighting considerable headroom for improvement, while PipeMFL-240K provides a reliable and challenging testbed to drive future research. As the first public dataset and the first benchmark of this scale and scope for pipeline MFL inspection, it provides a critical foundation for efficient pipeline diagnostics as well as maintenance planning and is expected to accelerate algorithmic innovation and reproducible research in MFL-based pipeline integrity assessment.

⌚ **Benchmark & Code:** github.com/TQSAIS/PipeMFL-240K

👉 **Data & Dataset Card:** huggingface.co/datasets/PipeMFL/PipeMFL-240K

*Tianyi Qu, Songxiao Yang, and Haolin Wang contributed equally to this research.

†Corresponding author: Yafei Ou (yafei@ist.hokudai.ac.jp).

CCS Concepts

- Computing methodologies → Object detection; • Applied computing → Engineering.

Keywords

Computer Vision, Object Detection, Magnetic Flux Leakage Detection, Dataset and Benchmark, Non Destructive Testing.

1 Introduction

Long-distance metal pipelines serve as critical infrastructure for the transportation of energy resources such as oil and natural gas, owing to their high efficiency, large capacity and ability to operate continuously across vast and remote terrains [29, 36]. With the majority of pipelines now entering a stable operational phase, ensuring their structural integrity and safety through regular inspection and maintenance has become increasingly imperative. As shown in Fig. 1, Magnetic Flux Leakage (MFL) detection operates by magnetizing the pipeline wall and detecting variations in magnetic flux caused by metal loss, weld anomalies, or other structural/component features [40]. Due to its high inspection speed, strong penetration capability and robustness in various operating conditions, MFL stands as one of the most widely adopted non-destructive testing (NDT) methods for in-line pipeline inspection [6], particularly for ferromagnetic pipelines and corrosion-related anomalies [25, 35].

The original pipeline MFL signal comprises three-axis data, among which the axial component exhibits the most significant features [10]. When transformed into pseudo-color maps, the resulting images reveal several domain-specific characteristics: (i) The upper and lower boundaries of the image are physically connected, forming a circular data structure. (ii) Certain categories frequently co-occur (e.g., valves and tees often appear within the same image, typically within an actual spatial distance of less than 5 meters). (iii) Target categories are highly correlated with their positional distributions in the image (e.g., corrosion is predominantly located near the pipeline bottom, while branches are mainly concentrated at the top). These domain-specific attributes remain largely underexplored in existing research. A systematic investigation and effective integration of such prior knowledge can establish a more robust and explainable foundation for the detection and diagnosis of MFL-based pipeline features.

1.1 Related Works

Early MFL defect detection [21, 33, 41] relied on traditional pattern recognition approaches and sliding-window matching, which suffered from poor generalization. Currently, Deep learning has become the predominant choice for MFL detection owing to its ability to automatically learn discriminative features from raw MFL images [9]. Table 1 summarizes related MFL object detection research with Deep Learning. Yang et al. [43] first introduced a CNN-based [16] approach using an SSD [24] Network, demonstrating the feasibility of casting defect localization as an object-detection task. Subsequent studies [7, 18, 42] increasingly prioritized real-time performance to keep pace with high-speed inline inspection. YOLO [30] family, such as YOLOv5 [12] and YOLOv8 [13], soon emerged as the mainstream solution, trading two-stage refinement for a lightweight, rapid-forward architecture that can be deployed

on edge devices with minimal memory and latency. The most recent innovations aim to recover the precision traditionally sacrificed in single-stage architectures. This has led to the integration of attention mechanisms [8], anchor-free prediction heads and lightweight convolutional blocks into YOLO-based frameworks, representing a concerted trend toward models that are both highly accurate and computationally efficient. Beyond architectural improvements, there is also a growing emphasis on advanced learning paradigms. Researchers are increasingly exploring techniques such as semi-supervised learning [47] and self-supervised learning [46] to reduce dependency on large-scale, fully annotated datasets. These methods leverage unlabeled or weakly labeled MFL data to improve model generalization, offering promising pathways to address annotation bottlenecks inherent in specialized industrial inspection tasks.

In parallel, datasets for MFL defect detection research have undergone significant quantitative and qualitative expansion. Early collections were typically limited to single-class metal loss localization. In contrast, contemporary datasets have broadened their scope to include auxiliary pipeline components such as welds and flanges, with label vocabularies now often encompassing more distinct categories [8, 22, 34, 42, 47]. This evolution is accompanied by marked improvements in data quality: spatial resolution has increased, and dataset volumes have grown from a few thousand to several tens of thousands of annotated images.

1.2 Scenario Challenges

Despite these significant advances in model architectures and learning paradigms, the transition of deep learning-based MFL analysis from research to robust field application is hindered by several persistent data-centric challenges, as illustrated in Fig. 1. (i) The field lacks a standardized, public benchmark dataset. Research continues to rely on privately collected data, which hinders reproducible comparisons and slows collective progress. (ii) The high cost of expert annotation severely limits dataset scale; most studies are validated on only thousands of images. This lack of large-scale validation undermines confidence in model robustness and generalization to diverse, real-world pipeline conditions. (iii) The annotation focus remains narrow. Although recent datasets include more categories, critical pipeline structural components (e.g., tees, valves, and bends) are often omitted. Accurate detection of these components is essential for spatially mapping detected defects to precise physical locations along the pipeline [38]. Their absence can lead to erroneous excavation decisions, resulting in substantial economic losses [45].

Besides, the MFL detection exhibits several inherent challenges, as shown in Fig. 1: (i) A severely long-tailed category distribution, where damage and defect objects are often hundreds or even thousands of times more frequent than most pipeline components, which can drive detectors to overfit to these dominant categories and lead to systematically degraded performance on rare yet safety-critical components. (ii) Large inter-class scale variation, as components are often tens of times larger than damage or defect regions, resulting in substantial size disparities that make it difficult for conventional detectors to simultaneously capture small defects and large structural components within a unified representation. (iii) High intra-class feature variability, particularly for the metal

Table 1: Summary of related works on pipeline MFL image detection.

Works	Year	Images	Image size [px×px]	Resolution [mm/px · °/px]	Objects	Number of Categories		Pipe Type	Dataset Accessibility
						Damage	Component		
Yang et al. [43]	2018	20,000	560×420	[· · 0.86]	3,100	1	2	In-service	✗
Yuksel et al. [44]	2023	540	-	-	100	1	0	In-service	✗
Zhao et al. [46]	2023	-	-	-	2,000	1	0	Experimental	✗
Han et al. [7]	2023	24,633	640×640	[· · 0.56]	-	1	0	Experimental	✗
Xu et al. [42]	2023	1,000	-×288	[· · 1.25]	2,483	2	3	In-service	✗
Han et al. [8]	2023	23,739	512×512	[· · 0.7]	-	1	2	In-service	✗
Shen et al. [34]	2024	841	432×288	[2 · 1.25]	-	1	2	Experimental	✗
Manzoor et al. [26]	2024	33,000	128×128	[· · 2.8125]	33,000	1	0	In-service	✗
Lin et al. [11]	2025	200	-	-	-	1	0	Experimental	✗
Wang et al. [39]	2025	2,550	200×200	[· · 1.8]	-	1	0	Both	✗
Li et al. [18]	2025	36,098	960×640	[4.16 · 0.56]	8,194	1	0	In-service	✗
Liu et al. [22]	2025	841	7,640×640	[0.27 · 0.56]	-	3	2	Both	✗
Zhao et al. [47]	2025	-	1,333×888	[· · 0.41]	7,898	1	6	Experimental	✗
This work	2026	240,320	5,000×2,400	[1 · 0.15]	191,530	4	8	In-service	✓

loss/corrosion cluster and valve. As corrosion depth progresses, the MFL color response of metal loss gradually evolves from light yellow to dark red, leading to substantial appearance differences between mild and severe corrosion. Furthermore, valves include both unidirectional and bidirectional types, whose MFL signatures differ markedly (unique elliptic or symmetric line). Such intra-class variability can significantly complicate robust feature learning.

1.3 Our Contributions

This work introduces PipeMFL-240K, a large-scale and multi-class object detection dataset of pipeline MFL images. It comprises 240,320 pseudo-color MFL images collected from 11 pipelines spanning approximately 1,480 km in total, with 191,530 labeled objects across 12 critical categories, including defects and key structural components. PipeMFL-240K establishes a much-needed benchmark for the MFL inspection community, providing a common ground for evaluating and comparing state-of-the-art object detection models. We expect this dataset to become a foundational resource for the advancement of industrial AI and domain-specific object detection research. Our key contributions are threefold:

- **The first large-scale and multi-class object detection dataset of pipeline MFL imaging.** PipeMFL-240K is the largest publicly available dataset for pipeline MFL-based object detection, comprising 240,320 MFL images and 191,530 labeled objects. Its scale and real-world origin ensure that model training with sufficient variety and practical relevance, which can advance the feasibility of data-driven inspection systems.
- **Fine-grained, multi-class annotations with detailed statistics.** PipeMFL-240K provides the most comprehensive set of object categories for MFL-based detection to date, with 12 categories covering damage types and structural components. Accurate detection of these components offers crucial spatial references, thereby facilitating the precise

localization of damage or defects in the physical space along the pipeline.

- **Comprehensive Benchmarking and Reproducible Experimental Framework.** We present a benchmark for multi-class object detection in pipeline MFL images, enabling standardized evaluation and comparison of algorithms for pipeline MFL detection.

2 Overview of Dataset

2.1 Image and Annotation

The dataset consists of 240,320 pseudo-color images from 11 different pipelines. The dataset is organized using the Portable Network Graphics (PNG) format. The detailed data pre-processing procedure is summarized in Section B.2.

Annotation is performed by a dedicated team consisting of six data analysis experts. This expert team has annotation experience for more than ten years. According to over 5,000 reports of real excavating testing statistics, the precision of the annotation exceeds 98%, which ensures that the annotations are both accurate and relevant for real-world engineering applications. The precision is not an intra-annotator k-value but the post-excavation confirmation rate obtained from the field reports of the pipeline operator. This engineering-based validation ensures that the bounding boxes are aligned with real-world defect confirmations rather than with purely academic consensus metrics.

The annotations consist of precise bounding-boxes for 4 types of damage and 8 types of component, including Metal Loss (MTL), Corrosion Cluster (CRC), Girth Weld Anomaly (GWA), Spiral Weld Anomaly (SWA), Bend (BND), Sleeve (SLE), Branch (BRN), Tee (TEE), Casing (CAS), Valve (VAL), External Support (ESP) and Flange (FLA). A more detailed problem formulation, along with category-wise example detections, is provided in Section B.3.

Fig. 2 presents an overview of the PipeMFL-240K dataset, highlighting the spatial distribution of various component types and damage categories along the pipeline. This global layout provides

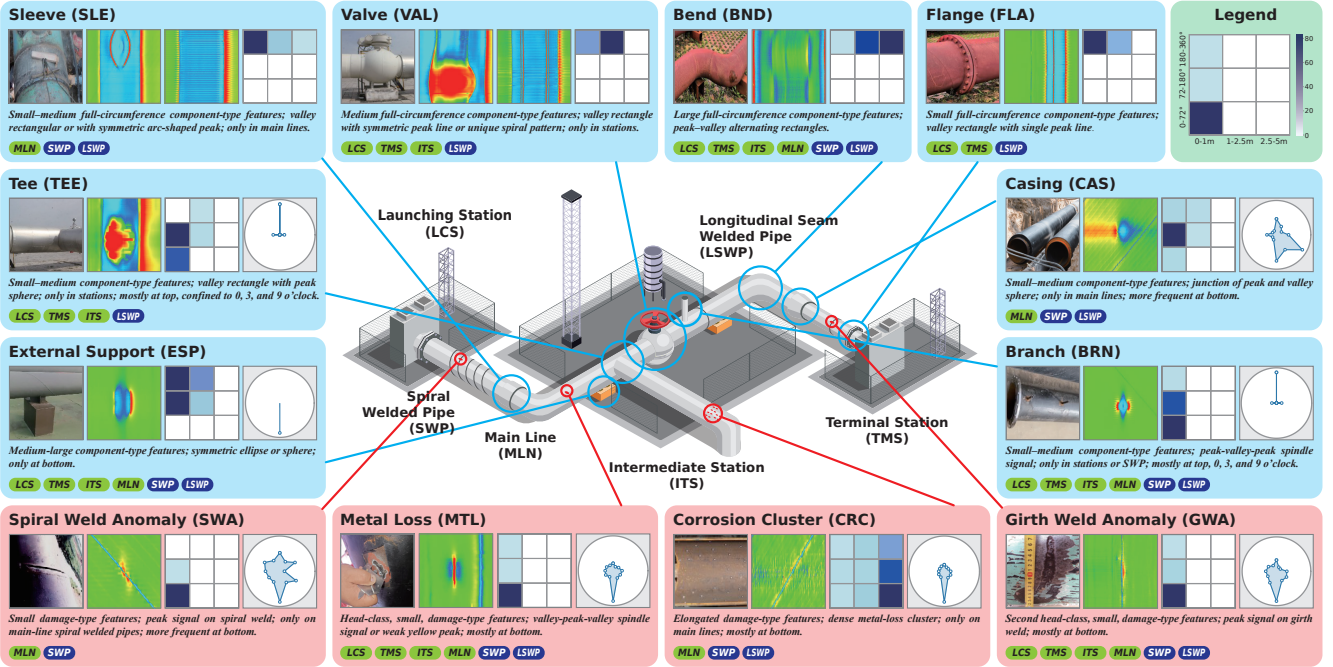


Figure 2: Feature taxonomy and annotation characteristics of the PipeMFL-240K dataset. The figure illustrates the pipeline topology and the complete label space used in the dataset. The central schematic provides the spatial context of in-line inspection, including launching, intermediate and terminal stations (LCS, ITS, and TMS) and main line (MLN), as well as different pipe types such as spiral welded pipe (SWP) and longitudinal seam welded pipe (LSWP). Surrounding panels present the annotated feature taxonomy. For each category, representative optical images and MFL signal maps are shown together with schematic circumferential signal patterns and occurrence distributions. The colored tags indicate the inspection contexts in which each category appears, highlighting the multi-context nature of the labels.

intuitive insight into where different structural elements and defect patterns are most likely to occur, thereby revealing the strong coupling between inspection context and object appearance.

PipeMFL-240K exhibits highly heterogeneous signal characteristics across categories. Component-related categories typically generate stable and repetitive MFL responses that are closely aligned with specific structural configurations. In contrast, damage-related anomalies tend to manifest as localized, low-contrast perturbations embedded within dominant background signals. Moreover, several damage categories share visually similar MFL signatures, which substantially increases inter-class ambiguity and renders fine-grained discrimination particularly challenging.

In addition, PipeMFL-240K demonstrates pronounced multi-context variability. While some categories consistently appear across diverse inspection positions and pipe segments, others are strongly constrained by local structural conditions. This interaction between category semantics and spatial context induces significant distributional imbalance and contributes to the long-tailed nature of the dataset. Consequently, effective learning on PipeMFL-240K necessitates models capable of jointly capturing signal appearance, structural priors, and spatial dependencies, rather than relying solely on isolated local features.

2.2 Statistics of PipeMFL-240K

We present a statistical analysis of the PipeMFL-240K dataset to characterize its category distribution, object density, and spatial contextual bias. Specifically, we analyze circumferential signal patterns and size distributions (Fig. 2) and examine category-level object counts, per-image object density, pipe-type distribution, and category-scenario distribution (Fig. 3). Additionally, we examine the relationship between pipeline attributes and category objects, as detailed in Section B.4.

Circumferential signal patterns (Fig. 2) indicate pronounced spatial contextual bias. Full-circumference component-type categories (SLE, VAL, BND, FLA) exhibit complete circumferential coverage, whereas several other component categories show clear azimuthal preferences (TEE and BRN are biased toward the top and concentrated near 0, 3, and 9 o'clock; CAS occurs only at 6 o'clock). Damage-type categories (SWA, CRC, GWA, MTL) are predominantly observed at 6 o'clock, corresponding to the bottom of the pipeline. In horizontal/stratified flow, free water preferentially wets and accumulates at the pipe invert, providing a persistent electrolyte and promoting the accumulation of solids and deposits [28]; under-deposit corrosion in such low areas is highly localized and accelerates metal loss [2]. Weld-related anomalies can be exacerbated

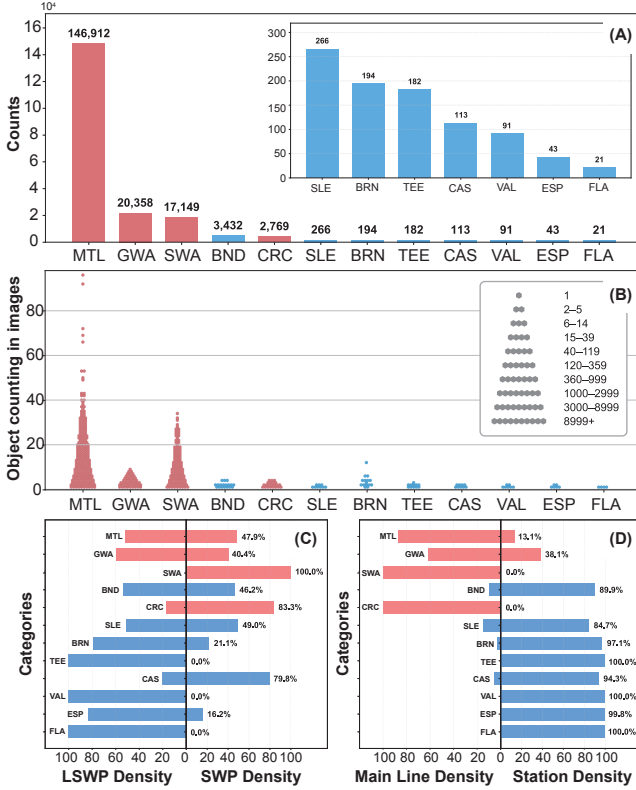


Figure 3: (A) Overall object counts for each annotated category, showing a highly long-tailed distribution across damage-type features (MTL, GWA, SWA, CRC) and component-type features (BND, SLE, BRN, TEE, CAS, VAL, ESP, FLA). **(B)** Distribution of object counting in images for each category, illustrating strong density imbalance, where a small subset of images contains a disproportionately large number of objects, particularly for metal loss and weld-related anomalies. **(C)** Relative density ratios of objects observed on LSWP versus SWP, revealing category-specific structural bias in pipe type. **(D)** Relative density ratios of objects appearing on main lines versus stations, highlighting pronounced contextual imbalance across inspection locations. Together, these statistics characterize the dataset as highly imbalanced in terms of category frequency, object density, and spatial context, posing significant challenges for learning robust and generalizable MFL inspection models.

by preferential weld corrosion mechanisms, particularly where welds intersect the bottom wetting zone [17].

Fig. 2 also provides category-wise size distributions, summarized on a 2D grid of axial length and circumferential coverage. Component-type categories are generally larger, whereas damage-type categories (MTL, GWA, SWA) are typically small and localized. CRC is an exception: it can be viewed as a spatially clustered MTL, representing regions where corrosion is dense and recurrent and thus tends to manifest itself as elongated areas of comparatively large extent. This extreme inter-class scale disparity substantially

increases the difficulty of detection, as models must simultaneously handle very large structural components and tiny damage signals within the same inspection imagery.

As shown in Fig. 3 (A), the dataset exhibits a highly long-tailed category distribution. Among damage-type anomalies, MTL dominates the dataset by a large margin, followed by GWA and SWA, while CRC is comparatively rare. Component-type features show substantially lower object counts overall, with BND, SLE and BRN being the most frequent and FLA and ESP appearing only sparsely. This pronounced imbalance reflects real-world inspection conditions, where certain types of defects occur much more frequently than others.

Fig. 3 (B) further analyzes the number of objects per image for each category. The results reveal a severe object-density imbalance, particularly for MTL and weld-related anomalies, where a small subset of images contains a very large number of objects. In contrast, most component-type features appear only a few times per image. This heavy-tailed density pattern indicates that learning algorithms must cope not only with category imbalance but also with large variations in object concentration across samples.

Spatial and structural biases are analyzed in Fig. 3 (C) and Fig. 3 (D). Fig. 3 (C) compares the relative density of objects on longitudinal seam welded pipes (LSWP) versus spiral welded pipes (SWP). Several categories exhibit strong pipe-type preference, indicating that their occurrence is tightly coupled with specific manufacturing structures. Fig. 3 (D) shows the distribution of objects between main lines and inspection stations. Component-type features are predominantly observed at stations, whereas damage-type anomalies are concentrated on main lines. This clear contextual separation highlights the multi-context nature of the dataset and the strong correlation between object categories and inspection locations.

3 Experiments and Benchmarks

3.1 Experimental Setup

Pseudo-color MFL images in PipeMFL-240K represent a full circumferential unwrap in the vertical direction and an axial scan in the horizontal direction, meaning the inspection data are inherently continuous along the pipe axis, and the axial extent is effectively unbounded compared with the fixed circumference. To reflect this deployment reality, a unified patch-based pipeline is adopted in which both training and inference operate on full-circumference square slices: each slice always covers the entire full circumferential context while moving along the axial direction. This design serves two goals: (i) it preserves geometry-dependent patterns of structural components that require complete circumferential context and (ii) it enables an evaluation that explicitly tests a detector's robustness and localization stability on continuous axial imagery, where defects can be sparse, tiny, and sensitive to boundary or context changes. The following paragraphs provide the exact training-time cropping, sampling strategy, and the sliding-window inference, merging procedure.

During training, two 2400×2400 windows with horizontal coordinates corresponding to 100-2500 and 2500-4900, are cropped from each 5000×2400 images and each window is then resized to 640×640 to match the detector input. To ensure stable training, we

Table 2: Object distribution across training, validation, and testing sets of PipeMFL-240K.

Dataset	Damage				Component								
	MTL	CRC	GWA	SWA	BND	SLE	BRN	TEE	CAS	VAL	ESP	FLA	Total
Training Set	87,617	1,630	12,191	10,244	2,049	154	99	113	60	48	25	13	114,243
Validation Set	29,575	566	4,032	3,482	675	54	50	31	28	20	9	4	38,526
Testing Set	29,720	573	4,135	3,423	708	58	45	38	25	23	9	4	38,761
Total	146,912	2,769	20,358	17,149	3,432	266	194	182	113	91	43	21	191,530

Table 3: Model comparison on PipeMFL-240K (Confidence score=0.25, IoU=0.5). The best results in each column are highlighted in bold and the second-best values are underlined.

Model	Year	mAP50	mAP50:95	Precision (macro, micro)	Recall (macro, micro)	F1-score (macro, micro)	Param [M]	FLOPs [G]
Faster R-CNN [31]	2017	0.106	0.060	0.065, 0.070	0.189, 0.065	0.091, 0.068	41.4	535.9
RetinaNet [19]	2017	0.173	0.086	0.111, 0.055	0.356, <u>0.467</u>	0.157, 0.098	32.4	519.8
YOLOv5-s [12]	2020	0.426	0.265	0.453, 0.377	0.564, 0.333	0.480, 0.354	9.1	23.9
YOLOv5-m [12]	2020	0.452	0.277	0.446, 0.388	0.577, 0.345	0.477, 0.365	25.1	64.0
YOLOv5-l [12]	2020	0.498	0.285	0.493, 0.377	<u>0.622</u> , 0.410	0.538, <u>0.393</u>	53.1	134.7
YOLOv8-s [13]	2023	0.402	0.248	0.413, 0.361	0.544, 0.369	0.449, 0.365	11.1	28.5
YOLOv8-m [13]	2023	0.450	0.288	0.448, 0.375	0.596, 0.356	0.490, 0.365	25.9	78.7
YOLOv8-l [13]	2023	0.475	0.298	0.529, 0.410	0.587, 0.368	<u>0.541</u> , 0.388	43.6	164.9
YOLO11-s [14]	2024	0.353	0.202	0.453, 0.376	0.485, 0.351	0.437, 0.363	9.4	21.3
YOLO11-m [14]	2024	0.406	0.251	0.511, 0.467	0.515, 0.297	0.488, 0.363	20.0	67.7
YOLO11-l [14]	2024	0.449	0.270	<u>0.583</u> , <u>0.469</u>	0.544, 0.273	0.529, 0.345	25.3	86.6
YOLOv8-s-world-v2 [4]	2024	0.467	0.297	0.444, 0.365	0.616, 0.375	0.493, 0.370	12.7	34.7
YOLOv8-m-world-v2 [4]	2024	0.494	0.327	0.533, 0.462	0.604, 0.298	0.535, 0.362	28.4	88.8
YOLOv8-l-world-v2 [4]	2024	0.469	<u>0.302</u>	0.507, 0.416	0.585, 0.386	0.530, 0.401	46.8	179.0
YOLOv8-x-world-v2 [4]	2024	0.498	0.300	0.613 , 0.504	0.585, 0.282	0.571 , 0.362	72.9	277.4
RT-DETR [48]	2024	0.174	0.074	0.253, 0.151	0.268, 0.400	0.238, 0.219	32.0	103.5
RF-DETR-Base [32]	2025	0.472	0.273	0.378, 0.151	0.650 , 0.514	0.460, 0.233	28.6	89.3
YOLO26-n [15]	2026	0.317	0.223	0.522, 0.394	0.397, 0.301	0.388, 0.342	2.4	9.5
YOLO26-s [15]	2026	0.432	0.251	0.474, 0.389	0.549, 0.312	0.472, 0.346	9.5	22.5
YOLO26-m [15]	2026	0.442	0.263	0.585, 0.436	0.550, 0.291	0.536, 0.349	20.4	67.9
YOLO26-l [15]	2026	0.363	0.210	0.616, 0.442	0.449, 0.279	0.475, 0.342	24.8	86.1
YOLO26-x [15]	2026	0.453	0.290	0.487, 0.398	0.575, 0.364	0.504, 0.380	55.6	193.4

maintain a foreground-to-background sampling ratio of 9:1 [14], while the validation and testing datasets remain unchanged. A slice is defined as a foreground sample if the patch center lies inside the bounding box of any annotated object; otherwise, it is treated as a background sample. In the training set, 53,375 patch slices contain objects and all of them are included in the training process. To make full use of the entire dataset, background patches are randomly sampled with sampling ratio 9:1, resulting in 5,930 background samples.

During inference, Slicing Aided Hyper Inference [1] is applied with a sliding window of 2400×2400 and a stride of 1300 px (45.8% overlap). Each slice is resized to 640×640 before being fed to the network; the resulting detections are mapped back to the original slice coordinates and merged across all windows via standard NMS [27] ($\text{IoU} [5] \geq 0.5$). Only boxes whose confidence exceeds 0.25 [14] are retained.

3.2 Implementation Setup

All experiments are performed on a server with $4 \times \text{RTX 4090}$ (24 GB), CPU Xeon Platinum 8470Q and 360 GB RAM. The dataset contains 240,320 pseudo-color MFL images, which are split into training/validation/testing sets with a ratio of 6:2:2. The object distribution is kept as balanced as possible in these splits, as summarized in Table 2. Each model is trained for 300 epochs with early-stopping of 20 epochs and the training process takes approximately one day per model. To guarantee fair comparison, the original hyperparameters released by each baseline repository are adopted without manual re-tuning; the only changes are dataset-specific input dimensions and batch size adjusted to fit GPU memory.

3.3 Benchmark Results

To evaluate MFL detection performance, comprehensive experiments are conducted on the PipeMFL-240K dataset, benchmarking

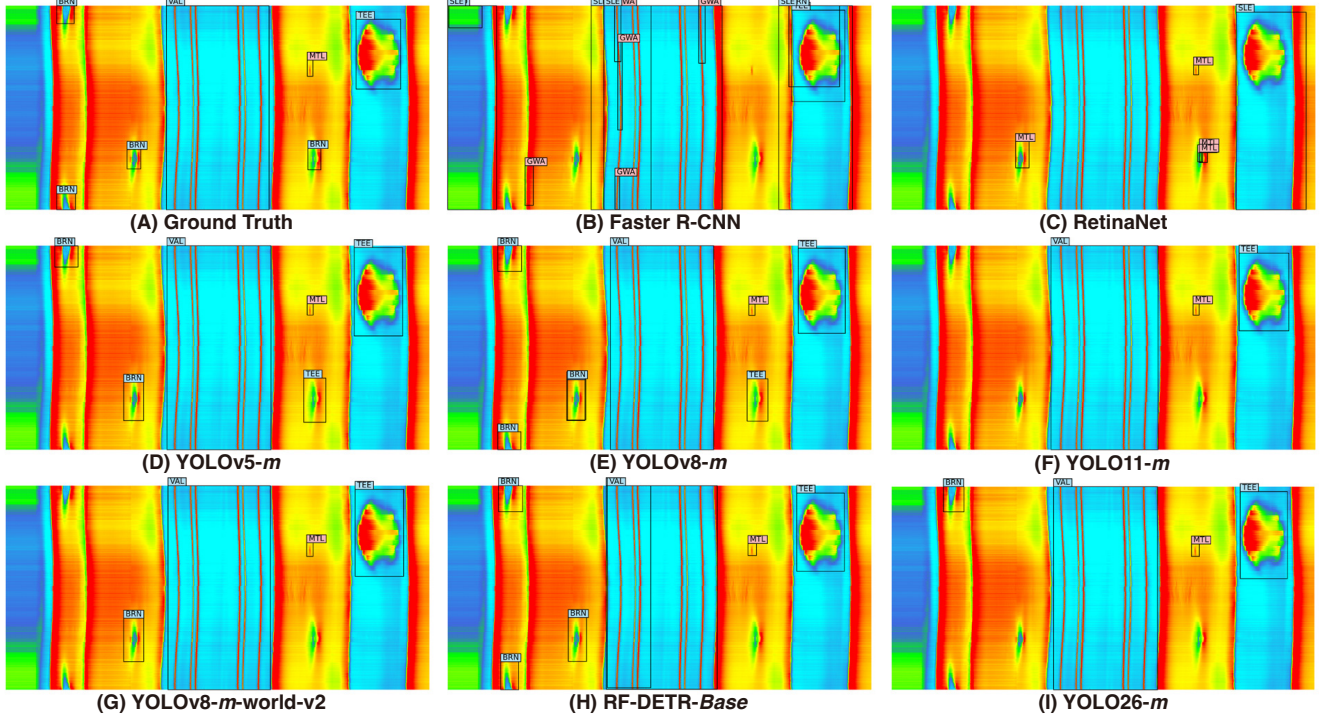


Figure 4: Qualitative benchmark results on representative MFL samples. Predicted bounding boxes from different detectors are compared under the same evaluation setting.

a series of widely-used supervised detection architectures. The supervised models encompassed: (i) Two-stage detectors: Faster R-CNN [31]; (ii) One-stage detectors: RetinaNet [19] and the YOLO series (YOLOv5 [12], YOLOv8 [13], YOLO11 [14], YOLO-World [4] and YOLO26 [15]); (iii) End-to-end transformers [37]: DETR-based [3] models (RT-DETR [48] and RF-DETR [32]).

Table 3 presents the benchmark comparison of all methods under the same evaluation setting. Detection accuracy is quantified following standard evaluation protocols using the COCO-style metrics [20]: mean Average Precision at $\text{IoU}=0.5$ (mAP₅₀), mean Average Precision at $\text{IoU}=0.50:0.05:0.95$ (mAP_{50:95}), Precision (P), Recall (R) and F1-score with macro and micro settings. Furthermore, model efficiency is assessed in terms of the number of parameters (Params) and computational complexity (FLOPs). The macro F1-score is the average of each category's F1-score, not calculated by macro P and R. Fig. 4 visualizes representative detection outputs for qualitative assessment. More detailed quantitative results (including per-category metrics) and additional qualitative visualizations are provided in Section C.1.

Among all tested benchmark models, the early one-stage model RetinaNet and the two-stage model Faster R-CNN have much more parameters than other models, but these models perform poorly. YOLO variants achieve superior accuracy-efficiency trade-offs, maintaining stable recall on dominant damage types and structural parts. Within the YOLO family, the YOLO-World series achieves the strongest results. Meanwhile, we notice that: (i) the latest release YOLO26, lags behind YOLOv8 and even YOLOv5, possibly because

its optimization revisions, loss redesign and end-to-end NMS-free inference do not align with MFL characteristics, while YOLOv8 and YOLOv5 have been upgraded and deployed in the field for a considerable period. (ii) As model size grows, performance typically improves from small to medium backbones but then saturates or fluctuates: further scaling yields diminishing returns and can even degrade certain metrics. Larger models also tend to adopt a noticeably more conservative decision boundary, consequently suppressing false positives more effectively and thus increasing precision at the expense of recall under a fixed threshold, while still achieving a higher overall F1-score in most cases.

DETR-based models are less competitive. Although RF-DETR approximates YOLO-level accuracy, RT-DETR fails to detect entire cohorts of categories, especially continuous structures such as VAL, SLE and FLA (Table 6-9 in Section C.1). The RT-DETR decoder lacks explicit global-scale reasoning, crippling the localization of elongated vertical components and dense micro-defects. Moreover, transformer detectors rely on pre-training over semantically balanced natural images; this prior conflicts with the heavily long-tailed MFL distribution, thereby limiting applicability to this task even further. Grounding-DINO [23] is evaluated under the same protocol; however, its results are omitted from Table 3 due to consistently poor performance. Zero-shot foundation models show limited transferability, as pre-training on natural imagery yields representations whose texture and semantic statistics diverge markedly from pseudo-color MFL maps; discriminative ability fails to transfer without domain-specific adaptation.

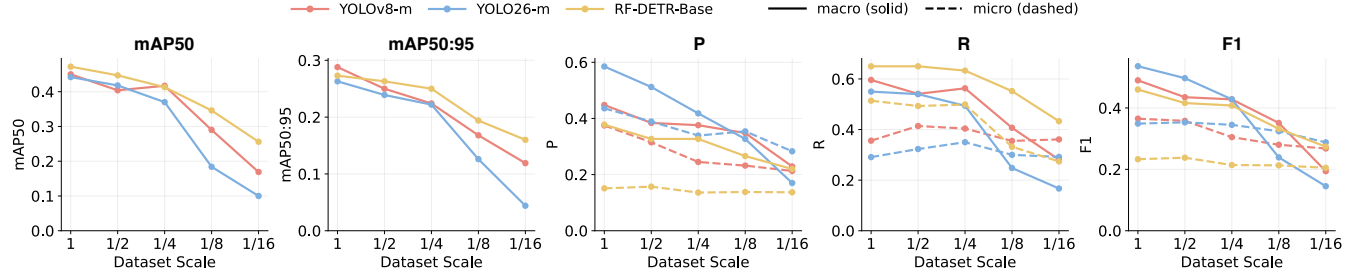


Figure 5: Dataset scale study results on YOLOv8-m, YOLO26-m and RF-DETR-Base, illustrating performance variations in mAP50, mAP50:95, precision, recall and F1-score as the training data decreases.

3.4 Data Scaling Study

To investigate the impact of data scale on model performance, we extract several subsets from the training set of PipeMFL-240K at different scales: 1/2, 1/4, 1/8, and 1/16. These subsets preserve approximately the same category distribution as the full training set, while ensuring that each category contains at least one object. Three models with moderate size are trained with these subsets: YOLOv8-m, YOLO26-m, and RF-DETR-Base. When the scale is less than 1/16, all models perform poorly ($mAP50 < 0.05$).

Fig. 5 demonstrates the performance of these models under different dataset scales: (i) $mAP50$, $mAP50:95$, Precision, Recall, and F1-score decrease when training with less data, indicating that a large-scale dataset is essential to achieve better detection performance. (ii) Among all models, RF-DETR-Base has the best robustness; when trained with only 1/16 of the data, the performance does not drop significantly, showing that RF-DETR-Base can be trained with insufficient samples. The per-category metrics of these models are summarized in Section C.2.

4 Discussion

We present a systematic investigation of complex-object detection in pipeline MFL imagery. The Benchmark results demonstrate the performance boundary of contemporary detectors on this task and reflect the structural challenges that MFL imaging possesses compared with natural scene images.

Challenge Analysis. Pipeline MFL detection exhibits clear, task-specific data and signal characteristics. (i) An extremely long-tailed category distribution induces severe imbalance, biasing training toward high-frequency categories and eroding sensitivity to infrequent yet safety-critical categories. (ii) Inter-class scale variance is drastic, head-type anomalies are spatially tiny and have a weak signal response, whereas tail-type features are large but rare, degrading precision. These properties require a unified architecture with exceptional scale generalization. Third, inter-class appearance variability is high, complicating stable feature learning. (iii) The categories are tightly coupled to pipe geometry and axial position in the vertical direction, suggesting that incorporating structural priors could be beneficial.

Baseline Comparison. Even with large-scale training data, mainstream detectors struggle to deliver consistent quality across all categories. The dominant performance bottleneck appears to stem

from a structural mismatch between prevailing detection paradigms and the characteristics of MFL data. Standard architectures implicitly assume relatively balanced categories and largely independent objects, whereas MFL imagery exhibits dense, position-dependent and severely imbalanced object distributions. Simultaneously localizing massive structural components and tiny defects further stresses the scale generalization of existing backbones. Moreover, purely data-driven feature learning neglects domain knowledge such as circumferential continuity, axial position priors and defect-scene associations, limiting both discrimination and stability.

5 Conclusion and Future Works

We present PipeMFL-240K, the first large-scale public dataset dedicated to pipeline MFL inspection, targeting the detection of both pipeline defect and component patterns in real inspection scenarios. The dataset provides a substantial collection of high-quality annotations, complemented by explicit pipeline type and scene metadata, enabling systematic analysis across diverse inspection conditions. In addition to dataset construction, we conduct a comprehensive benchmark study and statistical analysis, revealing pronounced long-tailed category distributions, extreme scale variation, and high intra-class diversity, which jointly characterize the intrinsic difficulty of MFL-based pipeline inspection. Benchmark results show that even state-of-the-art object detectors, including single-stage, two-stage, and Transformer-based architectures, achieve only limited performance on PipeMFL-240K. Performance degradation is particularly evident for rare categories and small-scale defects, highlighting unresolved challenges in current detection paradigms. These findings indicate that PipeMFL-240K exposes fundamental limitations of existing object detection methods under realistic industrial inspection conditions and provides a demanding evaluation platform for future research on robust detection under long-tailed distributions and severe multi-scale variations.

Future work should focus on improving robustness to category imbalance and scale variation in pipeline MFL inspection, with particular emphasis on rare and small-scale defects. In addition, exploring more efficient detection frameworks is important to support practical deployment, while more flexible labeling and detection paradigms may be considered to accommodate diverse and evolving inspection requirements.

Acknowledgments

This research was supported by National Natural Science Foundation of China (62573206, General Program), Science & Technology Research Special Fund of China National Machinery Industry Corporation (SINOMACH) and the Open Fund of National Engineering Research Center of Transducer (2025 No.5), China.

References

- [1] Fatih Cagatay Akyon, Sinan Onur Altinuc, and Alptekin Temizel. 2022. Slicing Aided Hyper Inference and Fine-tuning for Small Object Detection. *2022 IEEE International Conference on Image Processing (ICIP)* (2022), 966–970. doi:10.1109/ICIP46576.2022.9897990
- [2] Bruce Brown and Jeremy Moloney. 2017. Under-deposit corrosion. *Trends in oil and gas corrosion research and technologies* (2017), 363–383.
- [3] Nicolas Carion, Francisco Massa, Gabriel Synnaeve, Nicolas Usunier, Alexander Kirillov, and Sergey Zagoruyko. 2020. End-to-End Object Detection with Transformers. In *Computer Vision – ECCV 2020*, Andrea Vedaldi, Horst Bischof, Thomas Brox, and Jan-Michael Frahm (Eds.). Springer International Publishing, Cham, 213–229.
- [4] Tianheng Cheng, Lin Song, Yixiao Ge, Wenyu Liu, Xinggang Wang, and Ying Shan. 2024. YOLO-World: Real-Time Open-Vocabulary Object Detection. In *2024 IEEE/CVF Conference on Computer Vision and Pattern Recognition (CVPR)*. 16901–16911. doi:10.1109/CVPR52733.2024.01599
- [5] Mark Everingham, Luc Van Gool, Christopher Williams, John Winn, and Andrew Zisserman. 2010. The Pascal Visual Object Classes (VOC) challenge. *International Journal of Computer Vision* 88 (06 2010), 303–338. doi:10.1007/s11263-009-0275-4
- [6] Bo Feng, Jianbo Wu, Hongming Tu, Jian Tang, and Yihua Kang. 2022. A Review of Magnetic Flux Leakage Nondestructive Testing. *Materials* 15, 20 (2022). doi:10.3390/ma15207362
- [7] Fucheng Han and Xianming Lang. 2023. A Fast Magnetic Flux Leakage Small Defect Detection Network. *IEEE Transactions on Industrial Informatics* 19, 12 (2023), 11941–11948. doi:10.1109/TII.2023.3280950
- [8] Fucheng Han, Xianming Lang, and Mingyang Liu. 2023. An Anchor-Free Pipeline MFL Image Detection Method. *IEEE Transactions on Instrumentation and Measurement* 72 (2023), 1–8. doi:10.1109/TIM.2023.3304688
- [9] Songling Huang, Lisha Peng, Hongyu Sun, and Shisong Li. 2023. Deep Learning for Magnetic Flux Leakage Detection and Evaluation of Oil & Gas Pipelines: A Review. *Energies* 16, 3 (2023). doi:10.3390/en16031372
- [10] K. Hwang, S. Mandayam, S.S. Udupa, L. Udupa, W. Lord, and M. Atzal. 2000. Characterization of gas pipeline inspection signals using wavelet basis function neural networks. *NDT & E International* 33, 8 (2000), 531–545. doi:10.1016/S0963-8695(00)00008-6
- [11] Lin Jiang, Huaguang Zhang, Jinhai Liu, Xiangkai Shen, and Hang Xu. 2025. Mutual Supervision of MFL Heterogeneous Signals for Insufficient Sample Defect Detection on Pipeline Safety Operation. *IEEE Transactions on Automation Science and Engineering* 22 (2025), 1714–1724. doi:10.1109/TASE.2024.3369659
- [12] Glenn Jocher. 2020. *Ultralytics YOLOv5*. doi:10.5281/zenodo.3908559
- [13] Glenn Jocher, Ayush Chaurasia, and Jing Qiu. 2023. *Ultralytics YOLOv8*. <https://github.com/ultralytics/ultralytics>
- [14] Glenn Jocher and Jing Qiu. 2024. *Ultralytics YOLO11*. <https://github.com/ultralytics/ultralytics>
- [15] Glenn Jocher and Jing Qiu. 2026. *Ultralytics YOLO26*. <https://github.com/ultralytics/ultralytics>
- [16] Y. Lecun, L. Bottou, Y. Bengio, and P. Haffner. 1998. Gradient-based learning applied to document recognition. *Proc. IEEE* 86, 11 (1998), 2278–2324. doi:10.1109/5.726791
- [17] Chi-Ming Lee, S Bond, and P Woollin. 2005. Preferential weld corrosion: Effects of weldment microstructure and composition. In *CORROSION 2005*. Association for Materials Protection and Performance, 1–16.
- [18] Chunhui Li, Yan Lyu, Xianglai Meng, Linghui Li, and Xiaochen Pu. 2025. Research on Intelligent Defect Recognition in Oil and Gas Pipeline Magnetic Flux Leakage Detection Based on YOLOv8. *Chinese Journal of Scientific Instrument* 46, 2 (2025), 247–254.
- [19] Tsung-Yi Lin, Priya Goyal, Ross Girshick, Kaiming He, and Piotr Dollár. 2017. Focal Loss for Dense Object Detection. In *2017 IEEE International Conference on Computer Vision (ICCV)*. 2999–3007. doi:10.1109/ICCV.2017.324
- [20] Tsung-Yi Lin, Michael Maire, Serge Belongie, James Hays, Pietro Perona, Deva Ramanan, Piotr Dollar, and C. Lawrence Zitnick. 2014. Microsoft COCO: Common Objects in Context. In *Computer Vision – ECCV 2014*, David Fleet, Tomas Pajdla, Bernt Schiele, and Tinne Tuytelaars (Eds.). Springer International Publishing, Cham, 740–755.
- [21] Jinhai Liu, Mingrui Fu, Feilong Liu, Jian Feng, and Kuangqing Cui. 2018. Window Feature-Based Two-Stage Defect Identification Using Magnetic Flux Leakage Measurements. *IEEE Transactions on Instrumentation and Measurement* 67, 1 (2018), 12–23. doi:10.1109/TIM.2017.2755918
- [22] Jinhai Liu, Zhitao Wen, Xiangkai Shen, Fengyuan Zuo, Lin Jiang, and Huaguang Zhang. 2025. Online Pipeline Weld Defect Detection for Magnetic Flux Leakage Inspection System via Lightweight Rotated Network. *IEEE Transactions on Industrial Electronics* 72, 7 (2025), 7573–7584. doi:10.1109/TIE.2024.3503635
- [23] Shilong Liu, ZhaoYang Zeng, Tianhe Ren, Feng Li, Hao Zhang, Jie Yang, Chunyuan Li, Jianwei Yang, Hang Su, Jun Zhu, et al. 2023. Grounding dino: Marrying dino with grounded pre-training for open-set object detection. *arXiv preprint arXiv:2303.05499* (2023).
- [24] Wei Liu, Dragomir Anguelov, Dumitru Erhan, Christian Szegedy, Scott E. Reed, Cheng-Yang Fu, and Alexander C. Berg. 2016. SSD: Single Shot MultiBox Detector. In *Computer Vision – ECCV 2016 – 14th European Conference, Amsterdam, The Netherlands, October 11–14, 2016, Proceedings, Part I (Lecture Notes in Computer Science, Vol. 9905)*, Bastian Leibe, Jiri Matas, Nicu Sebe, and Max Welling (Eds.). Springer, 21–37. doi:10.1007/978-3-319-46448-0_2
- [25] Qingmiao Ma, Weige Liang, and Peiyi Zhou. 2025. A Review on Pipeline In-Line Inspection Technologies. *Sensors* 25, 15 (2025). doi:10.3390/s25154873
- [26] Mariam Manzoor, Zahra Arabi Narei, Henry Leung, and Scott Miller. 2024. Multi-Modal Pipeline Defect Localization. In *Muslims in ML Workshop co-located with NeurIPS 2024*. <https://openreview.net/forum?id=Mkkn1R6cCl>
- [27] A. Neubeck and L. Van Gool. 2006. Efficient Non-Maximum Suppression. In *18th International Conference on Pattern Recognition (ICPR'06)*, Vol. 3. 850–855. doi:10.1109/ICPR.2006.479
- [28] LD Paolini. 2018. Study of Phase Wetting in Three-Phase Oil-Water-Gas Horizontal Pipe Flow—Recommendations for Corrosion Risk Assessment. In *NACE CORROSION*. NACE, NACE–2018.
- [29] Xiang Peng, Uchechia Anyaoha, Zheng Liu, and Kazuhiko Tsukada. 2020. Analysis of Magnetic-Flux Leakage (MFL) Data for Pipeline Corrosion Assessment. *IEEE Transactions on Magnetics* 56, 6 (2020), 1–15. doi:10.1109/TMAG.2020.2981450
- [30] Joseph Redmon, Santosh Divvala, Ross Girshick, and Ali Farhadi. 2016. You Only Look Once: Unified, Real-Time Object Detection. In *2016 IEEE Conference on Computer Vision and Pattern Recognition (CVPR)*. 779–788. doi:10.1109/CVPR.2016.91
- [31] Shaoqing Ren, Kaiming He, Ross Girshick, and Jian Sun. 2017. Faster R-CNN: Towards Real-Time Object Detection with Region Proposal Networks. *IEEE Transactions on Pattern Analysis and Machine Intelligence* 39, 6 (2017), 1137–1149. doi:10.1109/TPAMI.2016.2577031
- [32] Isaac Robinson, Peter Robicheaux, Matvei Popov, Deva Ramanan, and Neehar Peri. 2025. RF-DETR: Neural Architecture Search for Real-Time Detection Transformers. *arXiv:2511.09554 [cs.CV]* <https://arxiv.org/abs/2511.09554>
- [33] M. Ruiz, L E Mujica, M. Quintero, J. Florez, and S. Quintero. 2015. Magnetic Flux Leakage and Principal Component Analysis for metal loss approximation in a pipeline. *Journal of Physics Conference Series* 628, 1 (2015).
- [34] Xiangkai Shen, Jinhai Liu, Lin Jiang, Xiaoyuan Liu, and Huaguang Zhang. 2024. A Novel Weld Defect Detection Method for Intelligent Magnetic Flux Leakage Detection System via Contextual Relation Network. *IEEE Transactions on Industrial Electronics* 71, 6 (2024), 6304–6314. doi:10.1109/TIE.2023.3294578
- [35] Yan Shi, Chao Zhang, Rui Li, Maolin Cai, and Guanwei Jia. 2015. Theory and application of magnetic flux leakage pipeline detection. *Sensors* 15, 12 (2015), 31036–31055.
- [36] Huadong Song, Qi Xiao, Gang Wang, Jianpeng Zhang, and Wenguang Hu. 2023. A Composite Approach of Electromagnetic Acoustic Transducer and Eddy Current for Inner and Outer Corrosion Defects Detection. *IEEE Transactions on Instrumentation and Measurement* 72 (2023), 1–11. doi:10.1109/TIM.2023.3238689
- [37] Ashish Vaswani, Noam Shazeer, Niki Parmar, Jakob Uszkoreit, Llion Jones, Aidan N Gomez, Łukasz Kaiser, and Illia Polosukhin. 2017. Attention is All you Need. In *Advances in Neural Information Processing Systems*, I. Guyon, U. Von Luxburg, S. Bengio, H. Wallach, R. Fergus, S. Vishwanathan, and R. Garnett (Eds.), Vol. 30. Curran Associates, Inc. https://proceedings.neurips.cc/paper_files/paper/2017/file/3f5ee243547dee91fb0d053c1c4a845aa-Paper.pdf
- [38] Jinzhu Wang and Zegen Wang. 2010. Defect Localization in Long-distance Oil and Gas Pipelines: A Survey. *Journal of Oil and Gas Technology* 372–374, 1 (2010), 3.
- [39] Qiannan Wang, Jianhua Tang, Jinhai Liu, Huaguang Zhang, Yifu Ren, Zhitao Wen, and Xiangkai Shen. 2025. A Novel Geometry-Aware Context Selection Network for Small Defect Detection Under Magnetic Flux Leakage Signals. *IEEE Transactions on Instrumentation and Measurement* 74 (2025), 1–12. doi:10.1109/TIM.2025.3571089
- [40] Jianbo Wu, Hui Fang, Xiaoming Huang, Hui Xia, Yihua Kang, and Chaoqing Tang. 2017. An Online MFL Sensing Method for Steel Pipe Based on the Magnetic Guiding Effect. *Sensors* 17, 12 (2017). doi:10.3390/s17122911
- [41] Lang Xianming, Zheng Hao, Song Huadong, Liu Jinhai, Guo Xiaoteng, Meng Qiang, and Yuan Haitao. 2021. Weld Defect Recognition Method of Pipeline Based on Improved Least Squares Twin Support Vector Machine. In *2021 29th Mediterranean Conference on Control and Automation (MED)*. 500–505. doi:10.1109/MED51440.2021.9480203
- [42] Zhenchang Xu, Kuirong Liu, and Kewei Gu, Xiaolu Gao. 2023. Image recognition model of pipeline magnetic flux leakage detection based on deep learning.

Corrosion Reviews 41, 6 (2023), 689–701.

[43] Lijian Yang, Zhujun Wang, and Songwei Gao. 2020. Pipeline Magnetic Flux Leakage Image Detection Algorithm Based on Multiscale SSD Network. *IEEE Transactions on Industrial Informatics* 16, 1 (2020), 501–509. doi:10.1109/TII.2019.2926283

[44] Veysel Yuksel, Yusuf Engin Tetik, Mahmut Omer Basturk, Onur Recepoglu, Kurşad Gokce, and Mehmet Ali Cimen. 2023. A Novel Cascaded Deep Learning Model for the Detection and Quantification of Defects in Pipelines via Magnetic Flux Leakage Signals. *IEEE Transactions on Instrumentation and Measurement* 72 (2023), 1–9. doi:10.1109/TIM.2023.3272377

[45] Luying Zhang, Yuchen Bian, Peng Jiang, Yang Huang, and Ying Liu. 2024. Improving Pipeline Magnetic Flux Leakage (MFL) Detection Performance With Mixed Attention Mechanisms (AMs) and Deep Residual Shrinkage Networks (DRSNs). *IEEE Sensors Journal* 24, 4 (2024), 5162–5171. doi:10.1109/JSEN.2023.3347510

[46] He Zhao, Jinhai Liu, Jianhua Tang, Xiangkai Shen, Senxiang Lu, and Qiannan Wang. 2023. A MFL Mechanism-Based Self-Supervised Method for Defect Detection With Limited Labeled Samples. *IEEE Transactions on Instrumentation and Measurement* 72 (2023), 1–10. doi:10.1109/TIM.2022.3212041

[47] He Zhao, Jinhai Liu, Huaguang Zhang, Qiannan Wang, Xiangkai Shen, and Xin Zhang. 2025. A Masked Multi-View Bidirectional Network for Class Extremely Imbalanced Object Detection Under Magnetic Flux Leakage Signals. *IEEE Transactions on Automation Science and Engineering* 22 (2025), 905–915. doi:10.1109/TASE.2024.3355984

[48] Yian Zhao, Wenyu Lv, Shangliang Xu, Jinman Wei, Guanzhong Wang, Qingqing Dang, Yi Liu, and Jie Chen. 2024. DETRs Beat YOLOs on Real-time Object Detection. In *2024 IEEE/CVF Conference on Computer Vision and Pattern Recognition (CVPR)*. 16965–16974. doi:10.1109/CVPR52733.2024.01605

A PipeMFL-240K Data Access and Format

The data can be accessed on Huggingface at <https://huggingface.co/datasets/PipeMFL/PipeMFL-240K>. The dataset has a permanent DOI: <https://doi.org/10.57967/hf/7651>. The benchmark and code can be accessed on Github at <https://github.com/TQSAIS/PipeMFL-240K>.

The dataset is organized in one main folder. The dataset structure is shown as follows:

```

PipeMFL-240K/
|-- train/
|   |-- images/           # Contains all train
|   |   |-- images in PNG format
|   |   |   |-- Train_A_0000011.png
|   |   |   |-- Train_A_0000047.png
|   |   |   |-- ...
|   |-- labels/           # Contains all train
|   |   |-- labels in TXT format (YOLO)
|   |   |   |-- Train_A_0000011.txt
|   |   |   |-- Train_A_0000047.txt
|   |   |   |-- ...
|   |-- train.coco.json   # Contains all train
|   |   |-- labels in JSON format (COCO)
|-- val/
|   |-- images/           # Contains all val
|   |   |-- images in PNG format
|   |   |   |-- Val_A_0000051.png
|   |   |   |-- Val_A_0000117.png
|   |   |   |-- ...
|   |-- labels/           # Contains all val
|   |   |-- labels in TXT format (YOLO)
|   |   |   |-- Val_A_0000051.txt
|   |   |   |-- Val_A_0000117.txt
|   |   |   |-- ...
|   |-- val.coco.json     # Contains all val
|   |   |-- labels in JSON format (COCO)
|-- test/
|   |-- images/           # Contains all test
|   |   |-- images in PNG format
|   |   |   |-- Train_A_0000086.png
|   |   |   |-- Train_A_0000096.png
|   |   |   |-- ...
|   |-- labels/           # Contains all test
|   |   |-- labels in TXT format (YOLO)
|   |   |   |-- Train_A_0000086.txt
|   |   |   |-- Train_A_0000096.txt
|   |   |   |-- ...
|   |-- test.coco.json    # Contains all train
|   |   |-- labels in JSON format (COCO)
|-- metadata_image.xlsx   # Image metadata of
|   |-- PipeMFL-240K
|-- metadata_pipe.xlsx    # Pipeline metadata
|   |-- of PipeMFL-240K
|-- data.yaml             # Pre-defined classes for
|   |-- PipeMFL-240K (YOLO)
|-- classes.txt           # Pre-defined classes for
|   |-- PipeMFL-240K (YOLO)

```

- PipeMFL-240K/{split}/labels/: Contains all the corresponding detection labels in train/val/test set stored in YOLO TXT format (.txt), with filenames matching the corresponding images.
- PipeMFL-240K/{split}/xxx.coco.json: Contains all the corresponding detection labels in train/val/test set stored in COCO JSON format (.json). The format of entries in JSON file is shown as follows:

```

{
  "categories": [
    {
      "id": 1,
      "name": "MTL",
    },
    {
      "id": 2,
      "name": "TEE",
    },
    {
      "id": 3,
      "name": "BND",
    },
    {
      "id": 4,
      "name": "CRC",
    },
    {
      "id": 5,
      "name": "BRN",
    },
    {
      "id": 6,
      "name": "GWA",
    },
    {
      "id": 7,
      "name": "SWA",
    },
    {
      "id": 8,
      "name": "ESP",
    },
    {
      "id": 9,
      "name": "VAL",
    },
    {
      "id": 10,
      "name": "FLA",
    },
    {
      "id": 11,
      "name": "CAS",
    },
    {
      "id": 12,
      "name": "SLE",
    }
  ]
  "images": [
    {

```

- PipeMFL-240K/{split}/images/: Contains all train/val/test images in PNG format. Each file is named as: [Split]_[PipelineID]_[ImageID].png

```

    "id": 0,
    "file_name": "Train_A_0000011.png",
    "width": 5000,
    "height": 2400
},
{
    "id": 1,
    "file_name": "Train_A_0000047.png",
    "width": 5000,
    "height": 2400
},
{
    "id": 2,
    "file_name": "Train_A_0000053.png",
    "width": 5000,
    "height": 2400
},
// ... other images (continued)
],
"annotations": [
{
    "id": 1,
    "image_id": 1,
    "category_id": 1,
    "bbox": [
        2911.0,
        330.0012,
        35.0,
        88.99920000000003
    ],
    "area": 3114.972000000001,
    "iscrowd": 0
},
{
    "id": 2,
    "image_id": 1,
    "category_id": 1,
    "bbox": [
        1347.0,
        1956.0012,
        31.0,
        70.9991999999997
    ],
    "area": 2200.975199999999,
    "iscrowd": 0
},
{
    "id": 3,
    "image_id": 2,
    "category_id": 1,
    "bbox": [
        1716.0,
        1703.000400000001,
        49.0,
        124.00080000000003
    ],
    "area": 6076.039200000001,
    "iscrowd": 0
},
// ... other annotations (continued)
]
}

```

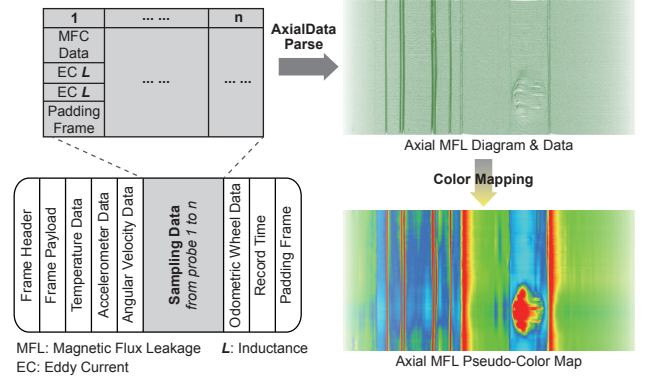


Figure 6: Overview of data collection and acquisition

- **data.yaml**: Contains pre-defined categories and data path for YOLO training.
- **classes.txt**: Contains pre-defined categories for result visualization with LabelImg for YOLO.
- **metadata_image.xlsx**: An Excel file containing mapping information (Pipe NO., Scene Type and Pipe Type) for each image.
 - **Image Name**: A string identifier following the pattern `Split_PipeNo_Index.png`, where `Split` denotes the dataset partition (Train, Val, or Test), `PipeNo` indicates the pipeline identifier (A-K), and `Index` is a 7-digit numeric identifier unique within each split and pipeline.
 - **Pipe No.**: A categorical identifier indicating the pipeline from which the image is acquired. Valid values are single uppercase letters (e.g., 240K-A, 240K-B, 240K-C, ..., 240K-K), each corresponding to a predefined pipeline.
 - **Scene Type**: A categorical variable specifying the scene category of the MFL image. Valid values include ITS, LCS, MLN and TMS.
 - **Pipe Type**: A categorical attribute indicating the pipeline type. Valid values include SWP and LSWP.
- **metadata_pipe.xlsx**: An Excel file containing information (Length, Diameter, Age, Probe Layout Type) for each pipeline.
 - **Pipe No.**: A unique identifier assigned to each pipeline segment in the dataset. The identifier consists of a dataset prefix 240K followed by an alphabetical suffix (e.g., 240K-A, 240K-B, 240K-C, ..., 240K-K) to distinguish individual pipelines.
 - **Length (km)**: The physical length of each pipeline, measured in kilometers (km).
 - **Diameter (mm)**: The nominal outer diameter of the pipeline, measured in millimeters (mm).
 - **Age (Year)**: The service age of the pipeline, expressed in years since commissioning.
 - **Probe Layout Type**: The sensor arrangement used in the MFL inspection detector. This field is a categorical variable indicating the probe layout configuration, with possible values including Single Row and Double Row.

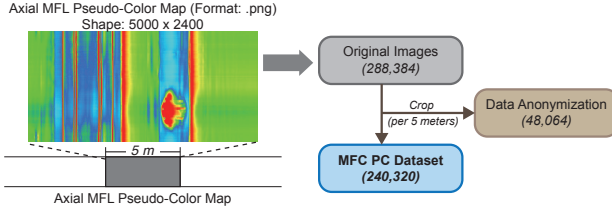


Figure 7: Overview of data selection and filtering.

B Detailed Information of PipeMFL-240K

B.1 License and Attribution

The pipeline MFL pseudo-color images and associated annotations (bounding-box annotations of features) in the dataset are licensed under the Creative Commons Attribution Non-Commercial 4.0 International License (CC BY-NC 4.0). For proper attribution when using this dataset in any publications or research outputs, please cite with the DOI: <https://doi.org/10.57967/hf/7651>. The benchmark and code can be accessed on GitHub at <https://github.com/TQSAIS/PipeMFL-240K>.

Suggested Citation: Qu, T., Yang, S., Wang, H., Song, H., Guo, X., Hu, W., Liu, G., Chen, H. & Ou, Y. (2026). PipeMFL-240K: A Large-scale Dataset and Benchmark for Object Detection in Pipeline Magnetic Flux Leakage Imaging. <https://doi.org/10.57967/hf/7651>

B.2 Data Pre-Processing

Collection and Acquisition. As shown in Fig. 6, during pipeline MFL inspection, the inspection detector travels along the axial direction of the pipeline while synchronously acquiring multi-channel sensor data. The raw data are organized in a frame-based format, with each frame comprising a frame header, padding information and detection signals from MFL, eddy current (EC) and inductance (L) sensors, together with motion-related measurements such as acceleration, angular velocity and odometer readings.

After acquisition, the raw frame data undergo axial data parsing and are reconstructed into a continuous MFL signal distribution referenced to the axial distance along the pipeline. By integrating odometer information for spatial mapping, an axial MFL data curve is generated. Subsequently, pseudo-color mapping is applied to convert the signal intensity into an intuitive two-dimensional pseudo-color representation, providing a unified data format for subsequent defect identification and analysis.

Selection and Filtering. As illustrated in Fig. 7, the complete pipeline pseudo-color images are cropped into fixed-size patches at intervals of 5 m. Each patch has a resolution of 5000 × 2400 pixels, resulting in a total of 288,384 images. Subsequently, 20% of the dataset is randomly removed to achieve data anonymization and conceal location-related information, corresponding to the exclusion of 48,064 images. After data filtering, the remaining 240,320 images constitute the PipeMFL-240K dataset.

B.3 Problem Formulation

The PipeMFL-240K consists of 240,320 pipeline magnetic flux leakage pseudo-color images with 191,530 objects of 12 categories. To

facilitate further research on the correlation between features and scenes, MFL images are categorized into 4 types of scenes and 2 types of pipeline. The definitions of each category, scene, and pipe type are as follows:

Damage. The core mission of this dataset is to detect these damage objects, including 4 types of features: metal loss (MTL), girth weld anomaly (GWA), spiral weld anomaly (SWA), and corrosion cluster (CRC). Fig. 8 illustrates the pseudo-color features of 4 damage-type categories. These categories have different distributions in sizes, shapes, colors, and patterns.

MTL: the most common type of damage in pipelines, characterized by local wall thinning or pitting. In MFL imaging, it typically appears as a blue-red-blue spindle-shaped structure or a light yellow spot or stripe. The affected regions are relatively small compared to the overall size of the image. MTL is commonly observed around the 6 o'clock direction (near the image center), corresponding to the bottom of the pipeline where corrosion tends to occur. It can appear in all scene types (LCS, TMS, ITS and MLN) and in both pipe types (LSWP and SWP).

CRC: the aggregation of a large number of closely distributed metal loss objects, forming an extensive corrosion region. CRC can only be found in the MLN scene and occurs in both LSWP and SWP pipe types. It is most commonly observed around the 6 o'clock direction (near the image center), corresponding to the bottom of the pipeline.

GWA: the anomaly occurring exclusively at the girth weld, which appears as a straight line spanning the vertical direction in an MFL image and results in local wall thinning at the girth weld. In MFL imaging, GWA is typically indicated by a light red or yellow response along the girth weld. It is most commonly observed around the 6 o'clock direction (near the image center), corresponding to the bottom of the pipeline. GWA can occur in any scene (LCS, TMS, ITS and MLN) and in both types of pipe (LSWP and SWP).

SWA: the anomaly occurring exclusively at the spiral weld, which appears as an inclined straight line spanning the vertical direction in an MFL image and results in local wall thinning at the spiral weld. In MFL imaging, SWA is typically indicated by a light red or yellow response along the spiral weld. It is most commonly observed around the 6 o'clock direction (near the image center), corresponding to the bottom of the pipeline. SWA only exists in the MLN scene with SWP pipe type.

Component. The core mission of this dataset is to detect these component objects, including 8 types of features: bend (BND), sleeve (SLE), branch (BRN), tee (TEE), casing (CAS), valve (VAL), external support (ESP) and flange (FLA). Fig. 9 presents the pseudo-color features of 8 component type categories. These categories also have distinct distributions in sizes, shapes, colors and patterns. In addition, most components exist in the station scene, with pipe type of LSWP, except BND, SLE and BRN.

BND: the pipeline component used to change the flow direction. In MFL imaging, BND typically appears as a very large valley-colored (blue or green) rectangular region spanning the vertical direction of the image, often accompanied by a symmetric peak-valley alternating pattern. BND can be found in any scene (LCS, TMS, ITS and MLN) and in both pipe types (LSWP and SWP).

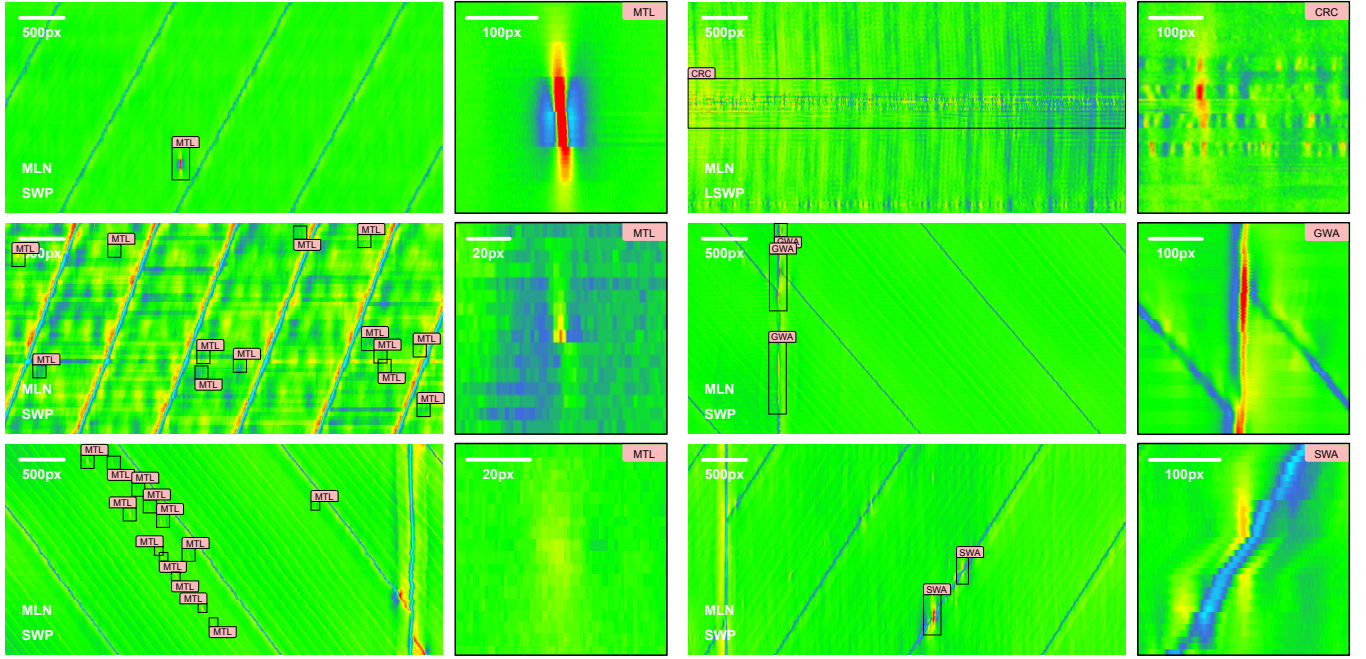


Figure 8: Pattern visualization of damage-type categories in MFL imaging cases: MTL, CRC, GWA and SWA with MLN scene and 2 pipe types (LSWP and SWP).

SLE: the component installed to repair, reinforce, isolate or adapt pipeline sections without replacing the entire line. In MFL imaging, SLE typically appears as a blue rectangular region spanning the vertical direction, with or without a symmetric elliptical pattern inside. SLE can only be found in the MLN scene and occurs in both LSWP and SWP pipe types.

BRN: the pipe component used to divert part of the fluid flow to other pipelines. In MFL imaging, BRN typically appears as a red-blue-red spindle-shaped structure. BRN can be found in any scenes, but only at positions 0, 3 and 9 o'clock.

TEE: the pipeline component used to control or split the flow direction. In MFL imaging, TEE typically appears as a light spherical region embedded within a darker rectangular region spanning the vertical direction of the image. TEE can be found in the LCS, ITS and TMS scenes with the LSWP pipe type and only at positions 0, 3 and 9 o'clock.

CAS: the component installed in a well to seal formation fluids, stabilize the well and maintain well integrity. In MFL imaging, CAS typically appears as a junction of adjacent red and blue spherical patterns. CAS can only be found in the MLN scene and occurs in both LSWP and SWP pipe types.

VAL: the component used to regulate fluid flow by opening, closing, or partially obstructing the pipeline. In MFL imaging, VAL typically appears as either a blue rectangular region with symmetric red lines spanning the vertical direction or as a distinctive spiral elliptical pattern. Both patterns extend across the vertical direction. VAL can only be found in station scenes (LCS, ITS and TMS).

ESP: the component used to prevent excessive settlement or sagging of the pipeline. In MFL imaging, ESP typically appears as a very large, vertically symmetric dark-colored pattern. ESP is

only observed at the 6 o'clock direction (near the image center), corresponding to the bottom of the pipeline and can occur in any scene, although it is most commonly found in station scenes.

FLA: the component that enables detachable and sealed connections between pipes, valves and equipment. In MFL imaging, FLA typically appears as a blue rectangular region spanning the vertical direction with a single red line along the vertical axis. FLA can only be found in the ITS and TMS scenes.

Scenes. To facilitate further research on the correlation between features and scenes, MFL images are categorized into 4 types of scenes: launching station (LCS), intermediate station (ITS), terminal station (TMS) and main line (MLN).

LCS: the launching station, representing the starting point of a pipeline and typically containing various pipeline components, with an approximate length of less than 100 meters. The pipe type in LCS is LSWP.

ITS: the intermediate station located along a long-distance transmission line, typically housing components such as valves and tees, with an approximate length of less than 50 meters. The pipe type in ITS is LSWP.

TMS: the terminal station, representing the end point of a pipeline and serving functions similar to a launching station for receiving operations. The pipe type in TMS is LSWP.

MLN: the main line scene, representing the most frequent operating condition in long-distance pipeline transmission, where damage types are frequently observed. The pipe type in MLN can be SWP or LSWP.

Pipeline types. To facilitate further research on the correlation between features and scenes, MFL images are categorized into 2

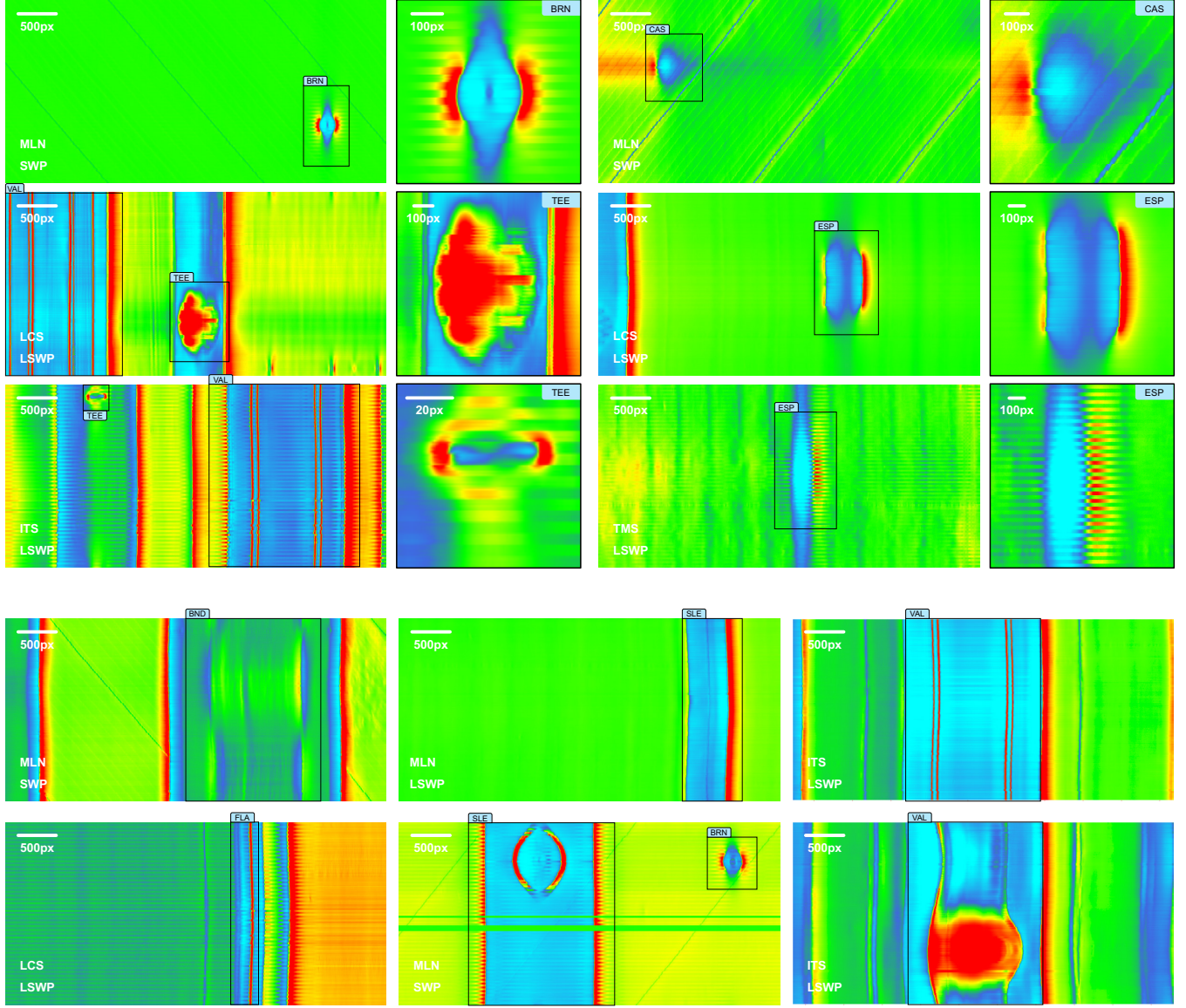


Figure 9: Pattern visualization of component-type categories in MFL imaging cases: BRN, CAS, TEE, ESP, BND, SLE, VAL and FLA with 4 scenes (LCS, ITS, TMS and MLN) and 2 pipe types (LSWP and SWP).

types of pipeline: longitudinal seam welded pipe (LSWP) and spiral welded pipe (SWP).

SWP: the pipe type containing spiral welds, which appear as inclined straight lines spanning the vertical direction in MFL images. Station-type scenes (LCS, ITS and TMS) do not exist in SWP.

LSWP: the pipe type that contains longitudinal seam welds and no spiral welds. Station-type scenes (LCS, ITS and TMS) exist only in LSWP. In addition, TEE, VAL and FLA are only observed in LSWP.

B.4 Overview of Data Distribution by Pipeline

From the perspective of individual pipelines, notable differences are observed in both the total number of objects and the category

composition, as shown in Table 5. Pipelines 240K-J, 240K-I and 240K-B contain relatively large numbers of annotated targets, whereas pipelines such as 240K-C, 240K-D and 240K-F have smaller sample sizes. These discrepancies are partly attributable to variations in pipeline length and inspection coverage and also reflect differences in service conditions and degradation levels among pipeline segments. Despite the pronounced imbalance in sample size across pipelines, their category distribution patterns are generally consistent with the overall trend of the dataset.

Furthermore, as shown in Table 4, substantial differences exist in the number of images and inspection mileage among pipelines, highlighting the strong heterogeneity in pipeline length and the

Table 4: Object distribution per pipeline in PipeMFL-240K.

Pipeline ID	Damage				Component								Total
	MTL	CRC	GWA	SWA	BND	SLE	BRN	TEE	CAS	VAL	ESP	FLA	
240K-A	13,221	1,241	41	563	90	13	45	2	0	4	4	3	15,227
240K-B	12,452	136	4,150	8,204	64	60	25	10	13	5	2	2	25,123
240K-C	6,300	259	1,440	300	82	24	20	10	15	3	2	3	8,458
240K-D	6,838	8	22	597	38	0	4	6	2	3	0	2	7,520
240K-E	11,257	806	536	1,511	312	9	6	14	0	3	1	2	14,457
240K-F	6,467	0	121	609	252	8	34	5	1	3	5	2	7,507
240K-G	6,245	49	3,170	736	1,440	15	12	35	12	8	15	2	11,739
240K-H	21,836	136	641	762	332	6	8	22	63	13	2	1	23,822
240K-I	21,650	87	4,888	332	282	1	4	23	3	10	4	1	27,285
240K-J	28,625	9	3,892	2,790	149	123	20	17	2	16	5	2	35,650
240K-K	12,021	38	1,457	745	391	7	16	38	2	23	3	1	14,742
Total	146,912	2,769	20,358	17,149	3,432	266	194	182	113	91	43	21	191,530

Table 5: Pipeline characteristics in PipeMFL-240K.

ID	Image	Density (Obj./m)	Length (km)*	Diameter (mm)	Age (year)
240K-A	12,304	0.218	70	457	20
240K-B	7,910	0.502	50	457	17
240K-C	6,871	0.211	40	457	17
240K-D	15,831	0.084	90	508	1
240K-E	12,640	0.180	80	610	16
240K-F	7,900	0.150	50	711	12
240K-G	38,690	0.049	240	711	8
240K-H	40,370	0.088	270	813	9
240K-I	26,614	0.182	150	813	9
240K-J	30,800	0.210	170	813	9
240K-K	40,390	0.055	270	813	9
Total	240,320	0.129	1,480	–	–

* To ensure data security and confidentiality, the dataset is de-identified: the approximate length of each pipeline is reported and approximately 80% of the images for each pipeline are randomly retained.

spatial distribution of defects. This characteristic closely aligns with the real-world engineering context of pipeline inspection, which is typically characterized by long distances and high heterogeneity. When normalized by pipeline length, the overall object density is 0.129 objects per meter, but with considerable variation across pipelines. The dataset covers pipeline diameters ranging from 457 to 813 mm and service lifetimes from 1 to 20 years. The correlation analysis reveals a significant positive correlation between object density and pipeline service age ($r = 0.6063$, 95% CI: 0.01008–0.8845, $p = 0.0480$), whereas no significant correlations are observed between object density and either pipeline diameter or pipeline length. This finding is consistent with engineering experience and established corrosion mechanisms, suggesting that corrosion defects

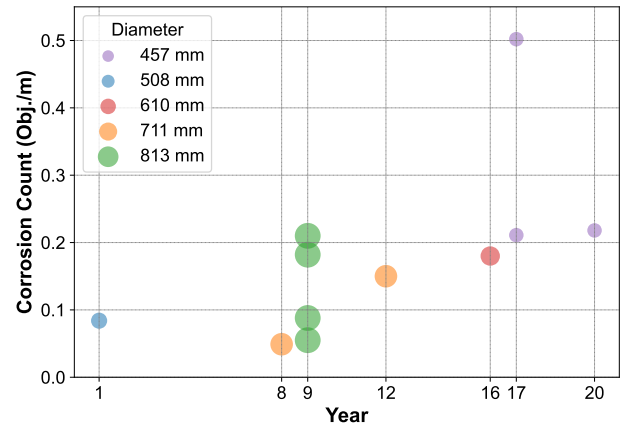


Figure 10: Corrosion density as a function of service age for pipelines with different diameters. Bubble sizes are scaled by diameter, illustrating the variation in corrosion occurrence across pipeline sizes over time.

tend to accumulate over time rather than being directly determined by geometric scale.

As illustrated in Fig. 10, the distribution of corrosion density is further analyzed along two dimensions: pipeline service age and diameter. From the temporal perspective, corrosion density exhibits an overall increasing trend with service age. During the early operational stage (approximately 1 year), corrosion density remains generally low, mostly below 100 objects per kilometer. In the mid-term stage (approximately 8–12 years), corrosion density begins to diverge markedly and differences among pipelines with varying diameters gradually become apparent. In the later stage of service (16–20 years), some pipeline segments exceed 200 objects per kilometer, with a few samples approaching or even reaching 500 objects per kilometer, indicating that long-term operation is a major driving factor for the rapid accumulation of corrosion

Table 6: Comparison of AP50 for each category in different models. The best results in each column are highlighted in bold and the second-best values are underlined. “-” indicates not detected.

Model	Damage					Component								Overall
	MTL	CRC	GWA	SWA	BND	SLE	BRN	TEE	CAS	VAL	ESP	FLA		
Faster R-CNN [31]	-	0.023	0.028	0.104	0.296	0.747	-	-	-	-	-	-	-	0.106
YOLOv8-s [13]	0.252	0.091	0.043	0.085	0.514	0.863	0.352	0.485	0.420	0.816	0.569	0.333	0.402	
YOLOv8-m [13]	0.243	0.113	0.051	0.090	0.571	0.871	0.362	0.771	0.531	<u>0.891</u>	0.651	0.250	0.450	
YOLOv8-l [13]	0.260	0.105	0.065	0.108	0.587	0.854	0.279	0.828	0.460	0.875	0.630	0.650	0.475	
YOLO11-s [14]	0.239	0.079	0.034	0.084	0.451	0.824	0.165	0.624	0.392	0.812	0.400	0.125	0.353	
YOLO11-m [14]	0.227	0.082	0.036	0.073	0.451	0.832	0.290	0.676	0.381	0.829	0.578	0.417	0.406	
YOLO11-l [14]	0.207	0.107	0.026	0.064	0.450	0.861	0.344	0.685	0.325	0.863	0.704	0.750	0.449	
YOLOv8-s-world-v2 [4]	0.256	0.102	0.054	0.099	0.568	0.838	0.408	0.830	0.547	0.857	0.547	0.510	0.467	
YOLOv8-m-world-v2 [4]	0.222	0.114	0.044	0.083	0.560	0.868	0.361	0.732	0.627	0.881	0.690	0.750	0.494	
YOLOv8-l-world-v2 [4]	<u>0.273</u>	0.132	0.076	0.131	0.559	0.848	0.394	0.825	<u>0.595</u>	0.919	0.750	0.125	0.469	
YOLOv8-x-world-v2 [4]	0.216	0.103	0.048	0.073	<u>0.577</u>	<u>0.878</u>	<u>0.435</u>	0.773	0.534	0.878	0.711	0.750	0.498	
RT-DETR [48]	0.202	0.020	0.035	0.075	0.361	-	0.374	0.894	0.122	-	-	-	0.174	
RF-DETR-Base [32]	0.246	0.128	0.070	0.108	0.501	0.810	0.479	<u>0.878</u>	0.365	0.849	0.477	0.750	0.472	
YOLO26-n [15]	0.202	0.093	0.019	0.064	0.489	0.840	0.308	0.208	0.240	0.844	-	0.500	0.317	
YOLO26-s [15]	0.212	0.136	0.027	0.079	0.494	0.861	0.405	0.684	0.460	0.840	0.333	0.650	0.432	
YOLO26-m [15]	0.206	0.149	0.032	0.088	0.430	0.829	0.346	0.775	0.452	0.864	0.386	0.750	0.442	
YOLO26-l [15]	0.200	0.120	0.024	0.065	0.445	0.836	0.300	0.519	0.360	0.759	0.222	0.500	0.363	
YOLO26-x [15]	0.256	<u>0.139</u>	0.044	0.108	0.567	0.880	0.399	0.599	0.444	0.833	0.477	0.688	0.453	

Table 7: Comparison of Precision for each category in different models. The best results in each column are highlighted in bold and the second-best values are underlined. “-” indicates not detected.

Model	Damage					Component								Overall
	MTL	CRC	GWA	SWA	BND	SLE	BRN	TEE	CAS	VAL	ESP	FLA		
Faster R-CNN [31]	-	0.015	0.076	0.101	0.152	0.436	-	-	-	-	-	-	-	0.065
RetinaNet [19]	0.068	0.012	0.020	0.023	0.281	0.130	-	0.189	0.103	0.320	0.188	-	-	0.111
YOLOv5-s [12]	0.402	0.112	0.312	0.292	0.441	0.632	0.638	0.709	0.409	0.790	0.500	0.200	0.453	
YOLOv5-m [12]	0.415	0.116	0.348	0.312	0.449	0.598	0.605	0.614	0.357	0.767	0.583	0.200	0.446	
YOLOv5-l [12]	0.391	0.147	0.296	0.313	0.479	0.634	0.650	0.714	0.484	0.793	0.636	0.375	0.493	
YOLOv8-s [13]	0.375	0.122	0.321	0.295	0.396	0.461	0.618	0.500	0.400	0.719	0.462	0.286	0.413	
YOLOv8-m [13]	0.401	0.111	0.339	0.269	0.451	0.639	0.609	0.689	0.329	0.789	0.500	0.250	0.448	
YOLOv8-l [13]	0.423	0.175	0.332	0.338	0.491	0.642	0.613	0.846	0.546	0.793	0.546	0.600	0.529	
YOLO11-s [14]	0.392	0.093	0.318	0.344	0.425	0.445	0.382	0.833	0.469	0.657	0.571	0.500	0.453	
YOLO11-m [14]	0.484	0.170	0.402	0.421	0.447	0.725	0.529	0.700	0.458	0.793	0.600	0.400	0.511	
YOLO11-l [14]	0.489	0.142	0.447	0.471	0.468	0.765	0.700	0.778	0.500	0.793	0.700	0.750	0.583	
YOLOv8-s-world-v2 [4]	0.384	0.105	0.301	0.321	0.443	0.604	0.641	0.800	0.419	0.677	0.294	0.333	0.444	
YOLOv8-m-world-v2 [4]	<u>0.493</u>	0.136	0.401	0.377	0.475	0.639	0.667	0.769	0.529	0.719	0.438	0.750	0.533	
YOLOv8-l-world-v2 [4]	0.428	0.231	0.310	0.382	0.464	0.708	0.641	0.821	0.500	0.793	0.382	0.333	0.507	
YOLOv8-x-world-v2 [4]	0.517	0.281	0.400	<u>0.455</u>	<u>0.498</u>	0.800	0.758	0.811	0.484	0.767	0.583	1.000	<u>0.613</u>	
RT-DETR [48]	0.174	<u>0.256</u>	0.108	0.057	0.508	-	0.667	0.875	0.389	-	-	-	-	0.253
RF-DETR-Base [32]	0.167	0.108	0.173	0.064	0.326	0.398	0.518	0.694	0.333	0.697	0.313	0.750	0.378	
YOLO26-n [15]	0.412	0.100	0.387	0.353	0.435	0.584	<u>0.739</u>	<u>0.889</u>	1.000	0.697	-	0.667	0.522	
YOLO26-s [15]	0.418	0.086	0.349	0.366	0.440	0.663	0.710	0.875	0.520	0.639	0.191	0.429	0.474	
YOLO26-m [15]	0.454	0.156	0.411	0.396	0.457	<u>0.781</u>	0.677	0.861	<u>0.750</u>	0.697	0.385	0.750	0.585	
YOLO26-l [15]	0.460	0.143	<u>0.427</u>	0.360	0.479	0.641	0.586	0.913	0.632	0.750	1.000	1.000	0.616	
YOLO26-x [15]	0.427	0.101	0.356	0.314	0.448	0.680	0.657	0.703	0.520	0.639	0.500	0.500	0.487	

defects. This evolutionary pattern is highly consistent with the

commonly observed “time-dependent degradation” behavior in MFL inspections.

Table 8: Comparison of Recall for each category in different models. The best results in each column are highlighted in bold and the second-best values are underlined. “-” indicates not detected.

Model	Damage				Component								Overall
	MTL	CRC	GWA	SWA	BND	SLE	BRN	TEE	CAS	VAL	ESP	FLA	
Faster R-CNN [31]	-	0.338	0.122	<u>0.403</u>	0.576	0.828	-	-	-	-	-	-	0.189
RetinaNet [19]	<u>0.524</u>	0.157	0.156	0.400	0.490	<u>0.914</u>	-	0.368	0.240	0.696	0.333	-	0.356
YOLOv5-s [12]	0.368	0.369	0.078	0.191	0.823	0.900	0.511	0.760	0.600	1.000	0.667	0.500	0.564
YOLOv5-m [12]	0.382	0.397	0.092	0.188	0.846	0.897	0.549	0.750	0.600	1.000	0.778	0.500	0.577
YOLOv5-l [12]	0.451	0.342	<u>0.168</u>	0.250	0.858	0.897	<u>0.578</u>	0.790	0.600	1.000	0.778	0.750	<u>0.622</u>
YOLOv8-s [13]	0.413	0.305	0.097	0.208	0.816	<u>0.914</u>	0.467	0.579	0.560	1.000	0.667	0.500	0.544
YOLOv8-m [13]	0.390	0.401	0.112	0.221	0.880	0.900	0.508	0.820	0.640	1.000	0.778	0.500	0.596
YOLOv8-l [13]	0.403	0.310	0.136	0.218	0.889	0.897	0.422	0.868	0.480	1.000	0.667	0.750	0.587
YOLO11-s [14]	0.400	0.263	0.074	0.175	0.754	<u>0.914</u>	0.289	0.658	0.600	1.000	0.444	0.250	0.485
YOLO11-m [14]	0.335	0.270	0.069	0.131	0.769	0.862	0.400	0.737	0.440	1.000	0.667	0.500	0.515
YOLO11-l [14]	0.308	0.317	0.046	0.108	0.761	0.897	0.467	0.737	0.360	1.000	0.778	0.750	0.544
YOLOv8-s-world-v2 [4]	0.415	0.415	0.125	0.205	0.859	0.948	0.556	0.842	0.720	1.000	0.556	0.750	0.616
YOLOv8-m-world-v2 [4]	0.326	0.362	0.085	0.153	0.880	<u>0.914</u>	0.489	0.790	0.720	1.000	0.778	0.750	0.604
YOLOv8-l-world-v2 [4]	0.419	0.324	<u>0.168</u>	0.245	<u>0.883</u>	0.879	0.556	0.842	0.680	1.000	0.778	0.250	0.585
YOLOv8-x-world-v2 [4]	0.309	0.247	0.096	0.126	0.872	0.897	0.556	0.790	0.600	1.000	0.778	0.750	0.585
RT-DETR [48]	0.446	0.035	0.160	0.325	0.561	-	0.489	0.921	0.280	-	-	-	0.268
RF-DETR-Base [32]	0.553	0.390	0.236	0.446	0.852	0.879	0.644	<u>0.895</u>	0.600	1.000	0.556	0.750	0.650
YOLO26-n [15]	0.346	0.284	0.033	0.138	0.738	0.897	0.378	0.211	0.240	1.000	-	0.500	0.397
YOLO26-s [15]	0.350	0.385	0.054	0.159	0.783	<u>0.914</u>	0.489	0.737	0.520	1.000	0.444	0.750	0.549
YOLO26-m [15]	0.322	0.368	0.059	0.169	0.748	0.862	0.467	0.816	0.480	1.000	0.556	0.750	0.550
YOLO26-l [15]	0.315	0.279	0.047	0.137	0.706	0.862	0.378	0.553	0.480	0.913	0.222	0.500	0.449
YOLO26-x [15]	0.402	<u>0.406</u>	0.094	0.231	0.829	<u>0.914</u>	0.511	0.684	0.520	1.000	0.556	0.750	0.575

Table 9: Comparison of F1-score for each category in different models. The best results in each column are highlighted in bold and the second-best values are underlined. “-” indicates not detected.

Model	Damage				Component								Overall
	MTL	CRC	GWA	SWA	BND	SLE	BRN	TEE	CAS	VAL	ESP	FLA	
Faster R-CNN [31]	-	0.029	0.094	0.161	0.240	0.571	-	-	-	-	-	-	0.068
RetinaNet [19]	0.121	0.023	0.035	0.043	0.356	0.227	-	0.250	0.145	0.438	0.240	-	0.157
YOLOv5-s [12]	0.384	0.172	0.125	0.231	0.574	0.742	0.567	0.734	0.487	0.882	0.572	0.286	0.480
YOLOv5-m [12]	0.398	0.157	0.146	0.235	0.586	0.716	0.542	0.675	0.447	0.868	0.667	0.286	0.477
YOLOv5-l [12]	<u>0.419</u>	0.205	<u>0.214</u>	<u>0.278</u>	0.615	0.743	<u>0.612</u>	0.750	0.536	0.885	<u>0.700</u>	0.500	0.538
YOLOv8-s [13]	0.393	0.175	0.148	0.244	0.533	0.613	0.532	0.537	0.467	0.836	0.545	0.364	0.449
YOLOv8-m [13]	0.395	0.174	0.168	0.243	0.596	0.747	0.554	0.749	0.434	0.882	0.609	0.333	0.490
YOLOv8-l [13]	0.413	0.224	0.193	0.265	<u>0.633</u>	0.748	0.500	<u>0.857</u>	0.511	0.885	0.600	0.667	<u>0.541</u>
YOLO11-s [14]	0.396	0.137	0.120	0.232	0.543	0.599	0.329	0.735	0.526	0.793	0.500	0.333	0.437
YOLO11-m [14]	0.396	0.209	0.117	0.199	0.563	0.787	0.456	0.718	0.449	0.885	0.632	0.444	0.488
YOLO11-l [14]	0.378	0.196	0.084	0.175	0.579	<u>0.825</u>	0.560	0.757	0.419	0.885	0.737	0.750	0.529
YOLOv8-s-world-v2 [4]	0.399	0.168	0.177	0.250	0.585	0.738	0.595	0.820	0.529	0.807	0.385	0.462	0.493
YOLOv8-m-world-v2 [4]	0.392	0.197	0.140	0.218	0.617	0.752	0.564	0.779	0.610	0.836	0.560	0.750	0.535
YOLOv8-l-world-v2 [4]	0.424	0.270	0.218	0.298	0.608	0.785	0.595	0.831	0.576	0.885	0.583	0.286	0.530
YOLOv8-x-world-v2 [4]	0.387	<u>0.263</u>	0.155	0.198	0.634	0.846	0.641	0.800	0.536	0.868	0.667	0.857	0.571
RT-DETR [48]	0.251	0.061	0.129	0.097	0.533	-	0.564	0.898	0.326	-	-	-	0.238
RF-DETR-Base [32]	0.256	0.169	0.200	0.112	0.472	0.548	0.574	0.782	0.429	0.821	0.400	0.750	0.460
YOLO26-n [15]	0.376	0.148	0.061	0.198	0.547	0.708	0.500	0.340	0.387	0.822	-	0.571	0.388
YOLO26-s [15]	0.381	0.140	0.093	0.221	0.564	0.768	0.579	0.800	0.520	0.780	0.267	0.546	0.472
YOLO26-m [15]	0.377	0.219	0.103	0.237	0.567	0.820	0.553	0.838	<u>0.585</u>	0.821	0.455	0.857	0.536
YOLO26-l [15]	0.374	0.189	0.085	0.198	0.571	0.735	0.459	0.688	0.545	0.824	0.364	0.667	0.475
YOLO26-x [15]	0.414	0.161	0.149	0.266	0.581	0.779	0.575	0.693	0.520	0.780	0.526	0.600	0.504

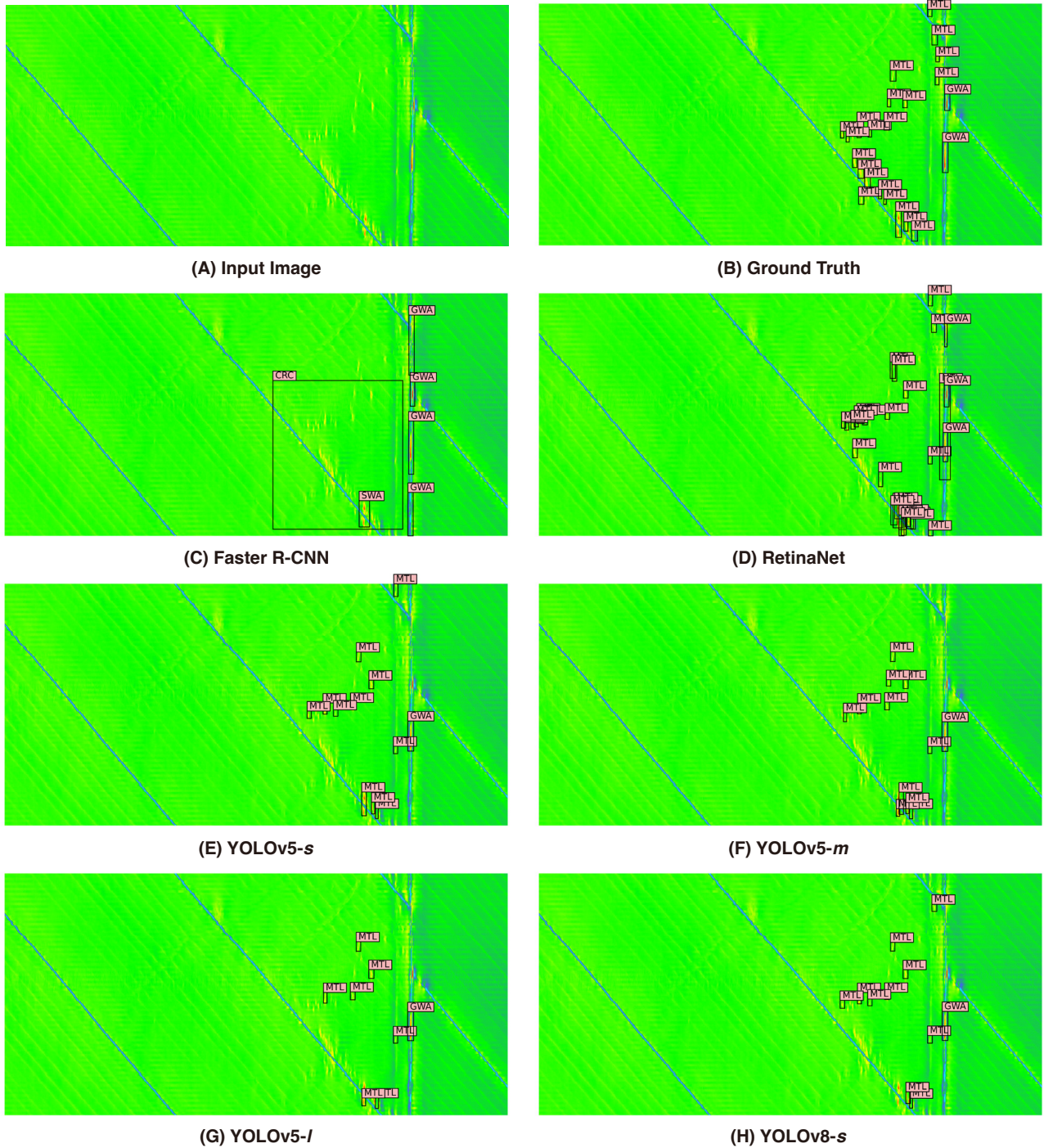


Figure 11: Qualitative benchmark results on representative damage samples (Part A).

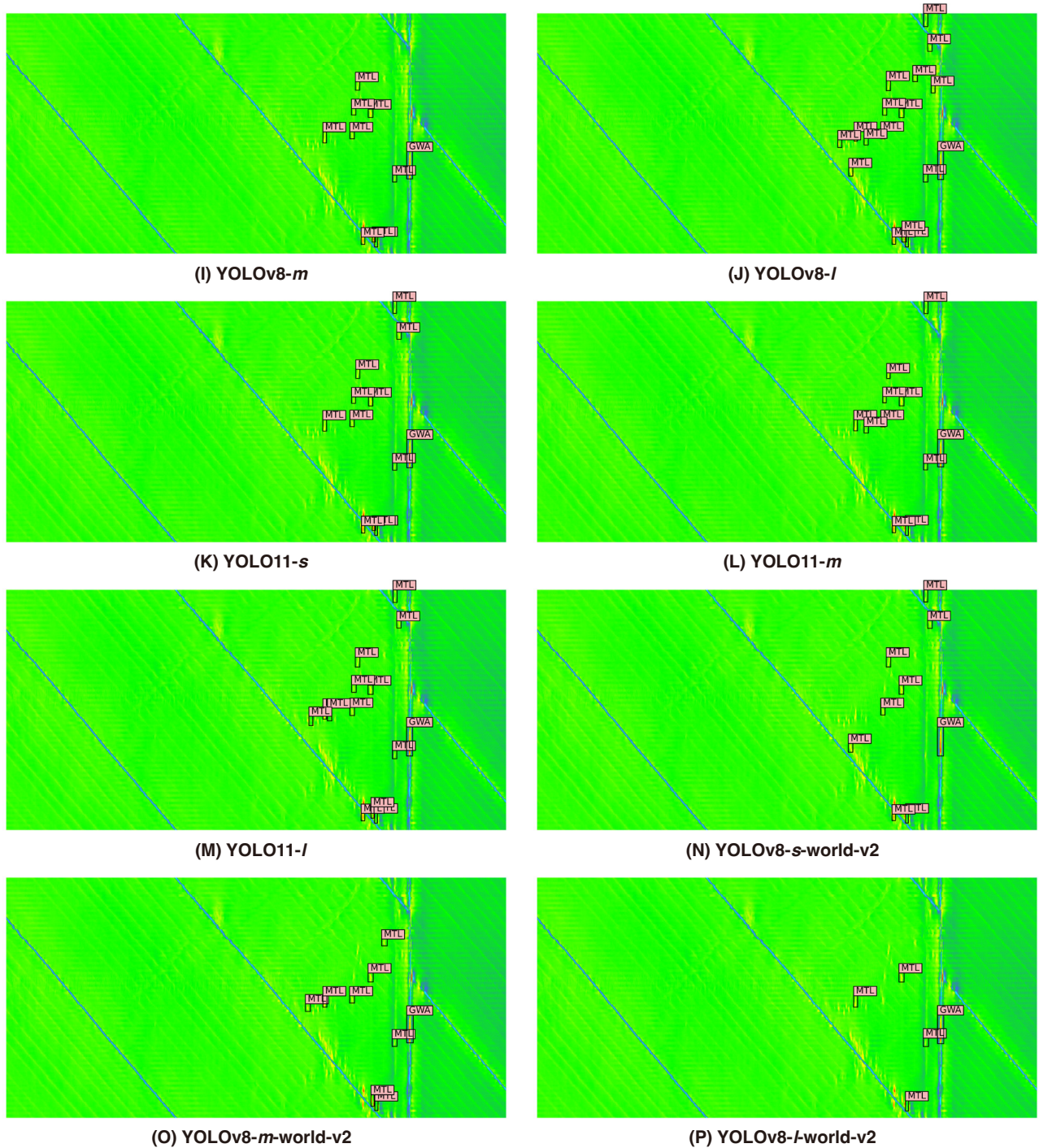


Figure 12: Qualitative benchmark results on representative damage samples (Part B).

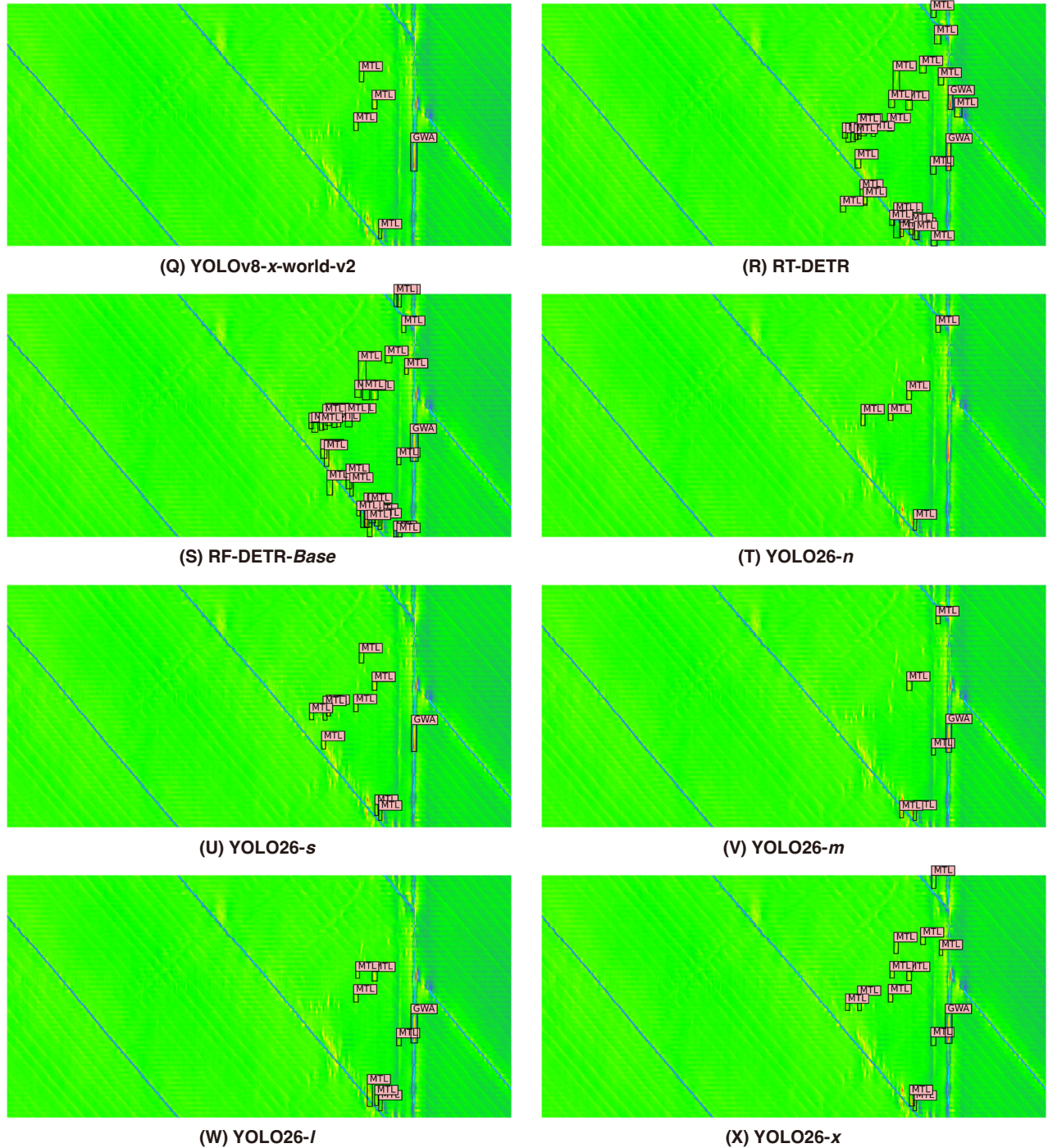


Figure 13: Qualitative benchmark results on representative damage samples (Part C).

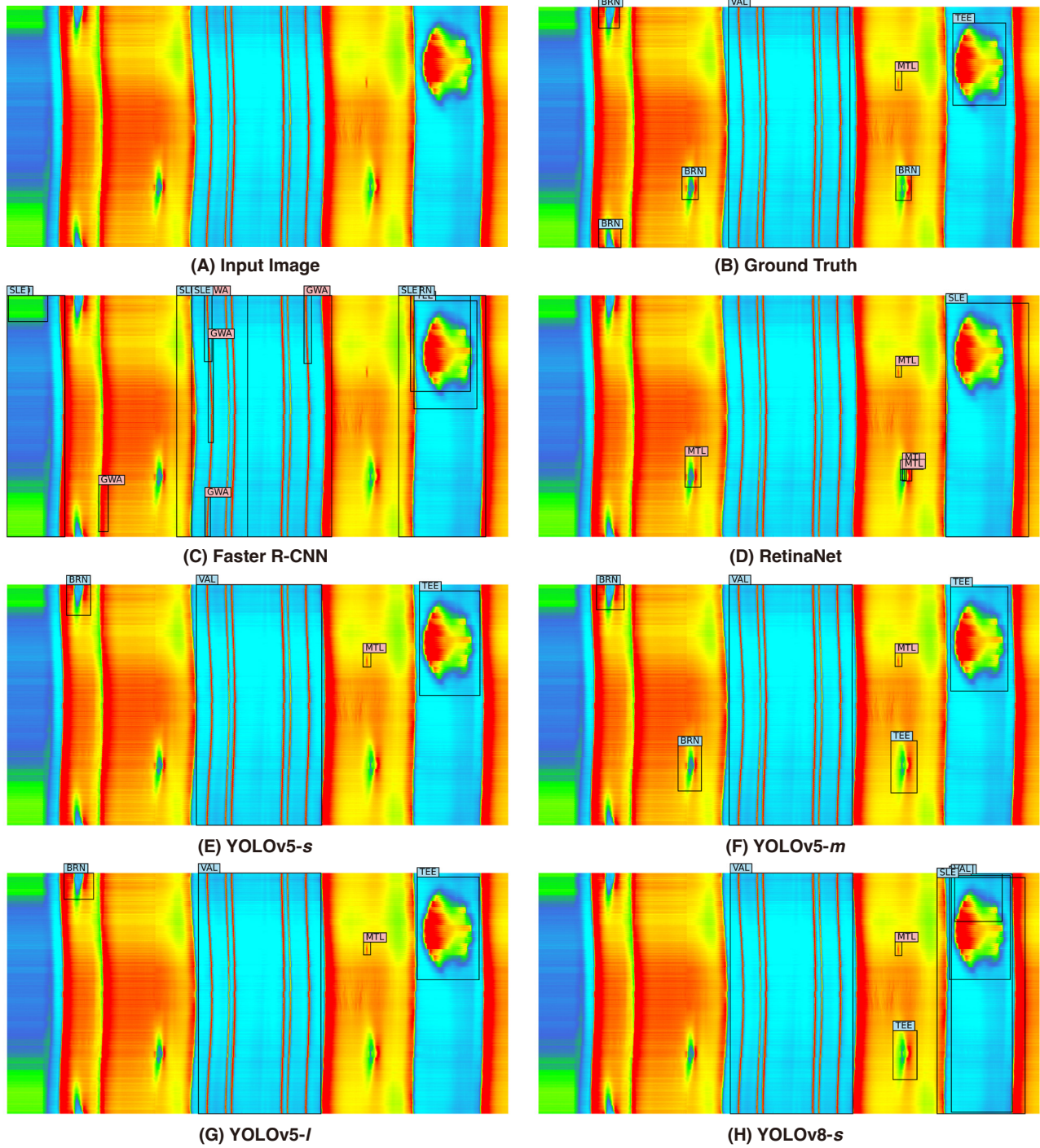


Figure 14: Qualitative benchmark results on representative component samples (Part A).

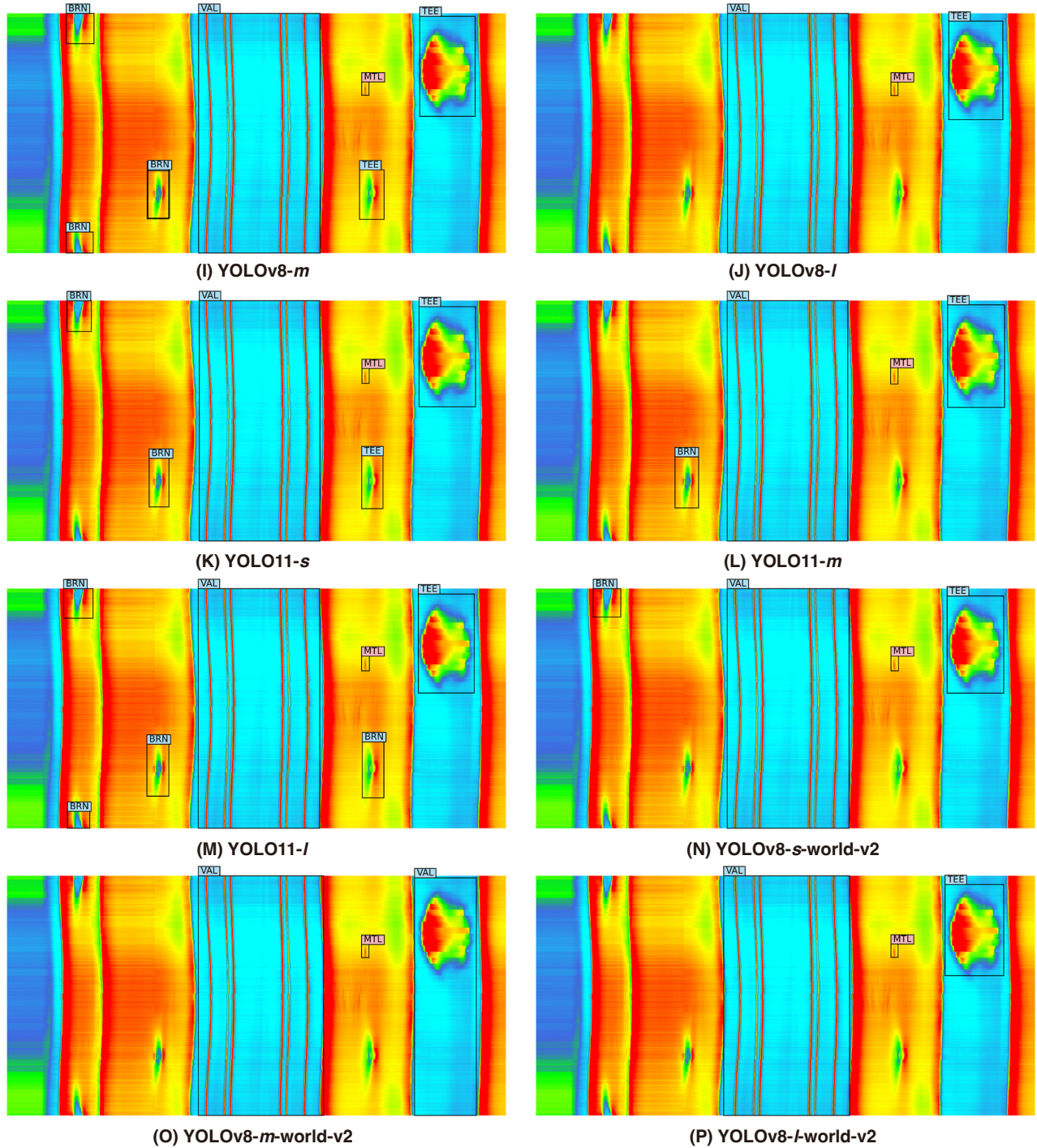


Figure 15: Qualitative benchmark results on representative component samples (Part B).

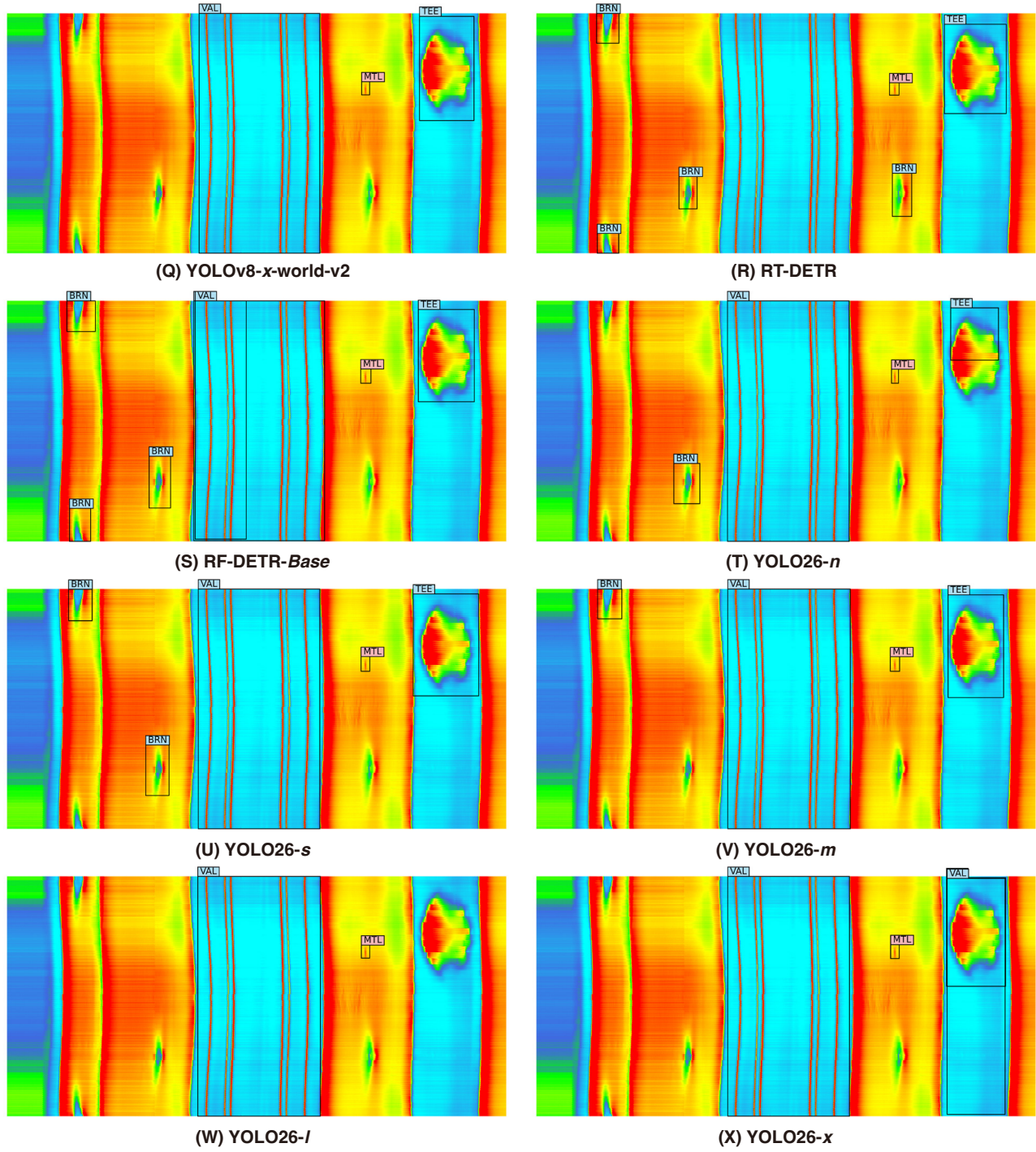


Figure 16: Qualitative benchmark results on representative component samples (Part C).

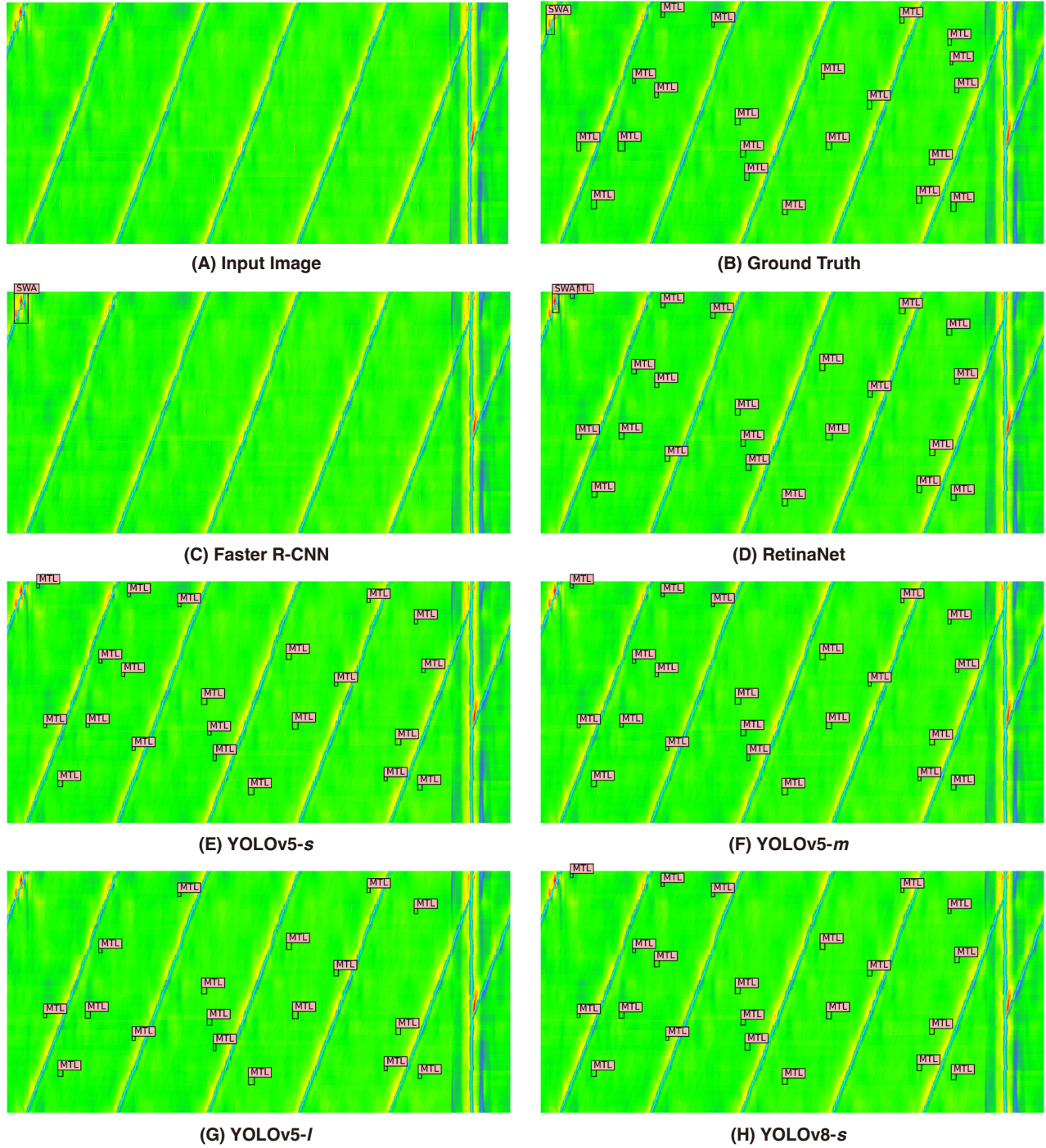


Figure 17: Qualitative benchmark results on representative tiny damage samples (Part A).

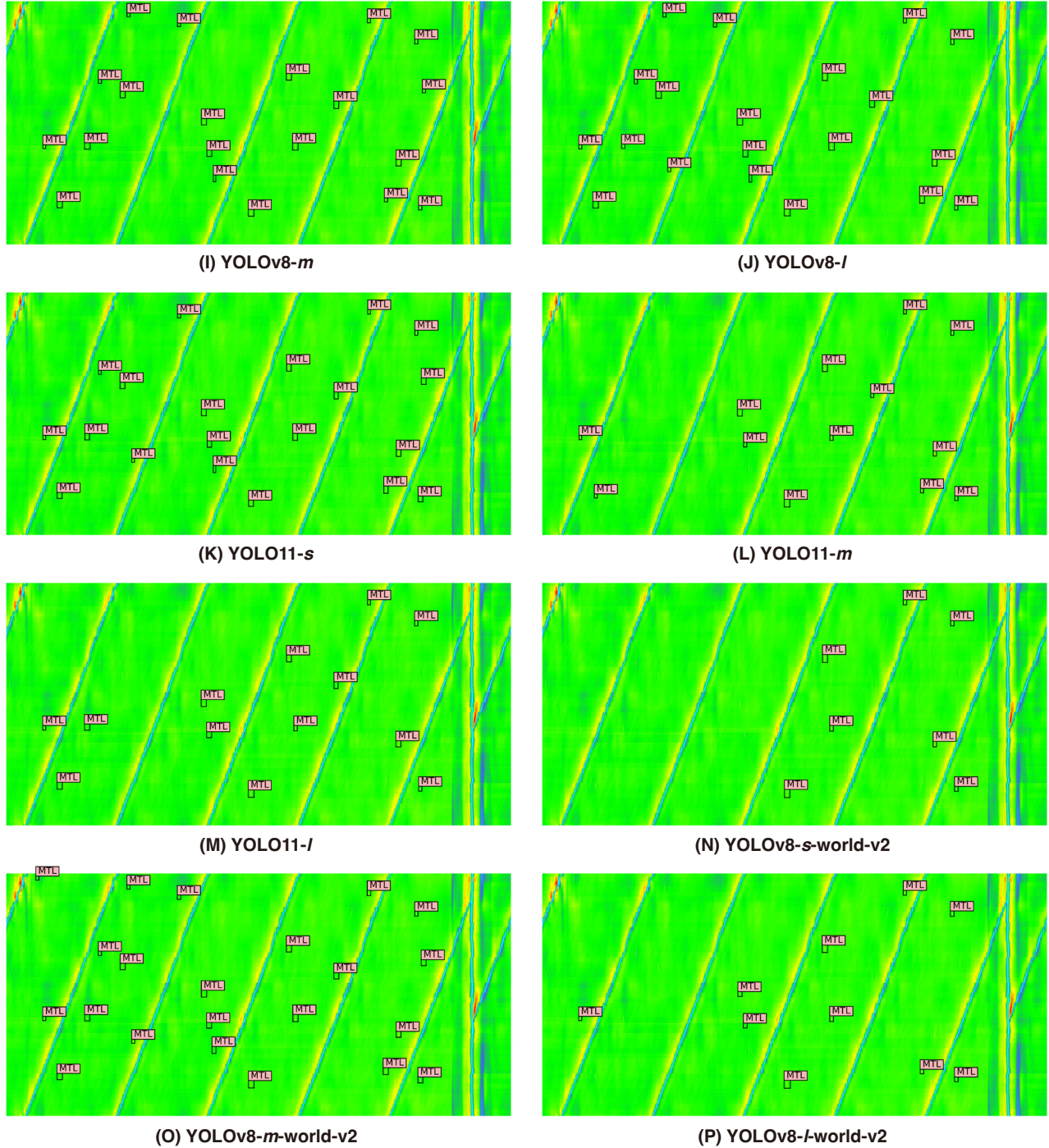


Figure 18: Qualitative benchmark results on representative tiny damage samples (Part B).

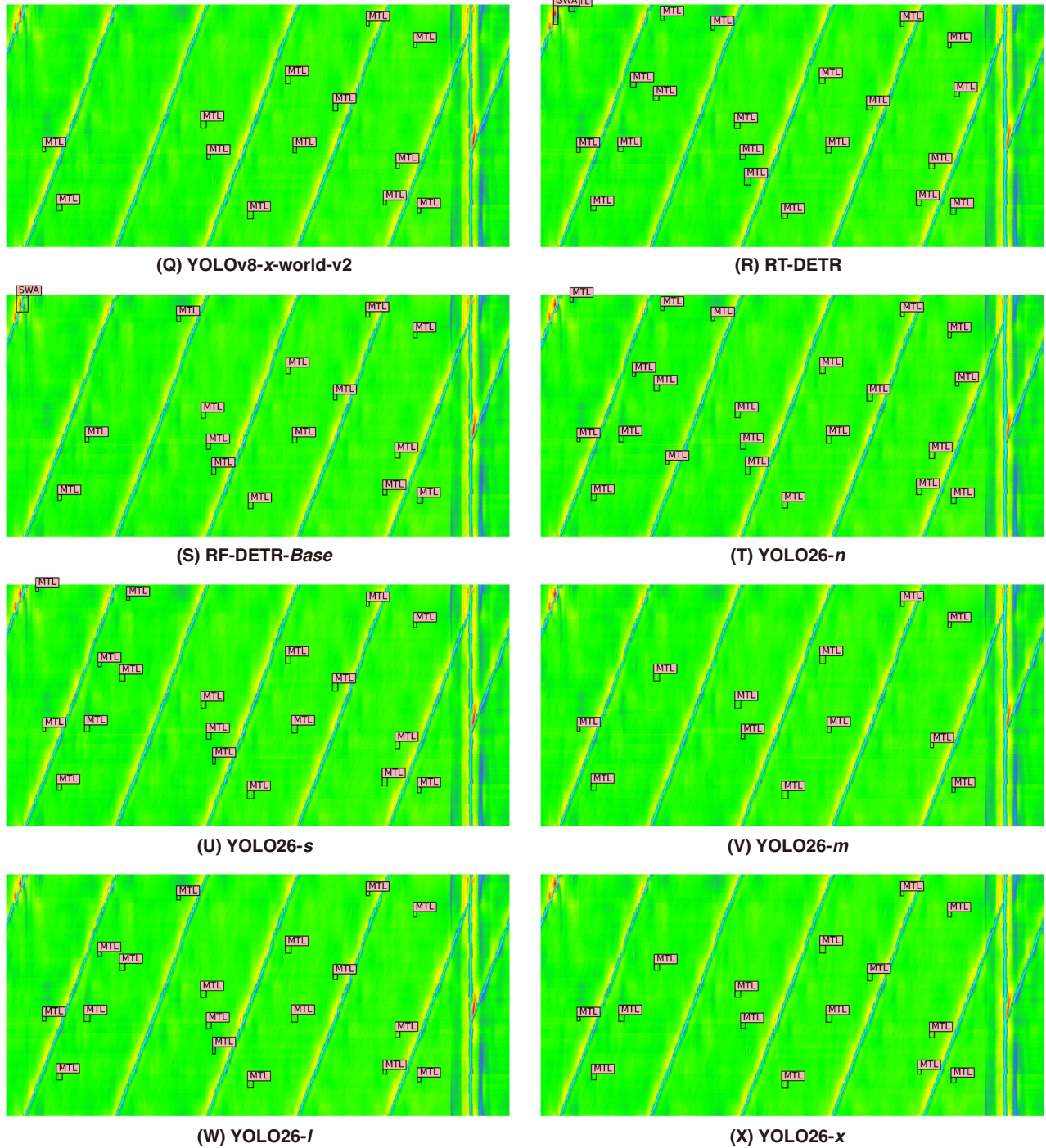


Figure 19: Qualitative benchmark results on representative tiny damage samples (Part C).

From the perspective of diameter effects, larger-diameter pipelines (e.g., 813 mm and 711 mm) already exhibit relatively high corrosion densities during the mid-term service stage, reaching approximately 180–210 objects per kilometer at around 8–9 years. This observation suggests that pipelines with larger diameters may be exposed to more complex corrosion environments under equivalent service durations, or alternatively, that their larger effective inspection area leads to the identification of more detectable defects. Meanwhile, smaller-diameter pipelines (457 mm) show pronounced peaks in corrosion density at later service stages (17–20 years), with one pipeline segment approaching nearly 500 objects per kilometer. This finding indicates that once small-diameter pipelines enter an accelerated degradation phase during long-term operation, the growth rate of defects can become extremely steep.

B.5 Dataset Maintenance

As the authors and maintainers of this dataset, we affirm that while the dataset is self-contained and does not depend on any external links or content, we may provide future updates, such as adding new cases or incorporating additional tasks. These potential updates aim to enhance the value of dataset while maintaining its long-term usability.

C Detailed Analysis of Experimental Results

C.1 Benchmark Results

C.1.1 Overall Performance Summary.

Table 3, 6–9 present the overall and per-category performance of each model, in terms of mAP50, mAP50:95 Precision, Recall and F1-score. The evaluation reveals a clear performance hierarchy across architectural families. The YOLOv8-World-v2 series achieves the highest overall mAP50 (**0.498**) and mAP50:95 (**0.327**). Early two-stage detectors such as Faster R-CNN and RetinaNet struggle with the extreme category imbalance and scale variance inherent to MFL images, achieving mAP50 below 0.2 and showing pronounced precision-recall imbalance. YOLO variants demonstrate balanced precision-recall profiles, while transformer-based detectors exhibit polarized behaviors. RF-DETR achieves the highest macro-recall (**0.650**) but suffers from low precision (0.378), whereas RT-DETR demonstrates complete category omission on continuous structural components (SLE, VAL, FLA achieve 0 AP50) despite excelling on discrete components such as TEE (AP50=**0.894**). Within the YOLO family, detection performance exhibits a positive correlation with model capacity, where scaling up from small to extra-large variants (e.g., model-s → model-l, YOLOv5, YOLOv8, YOLO11) generally yields consistent improvements in both mAP50 and mAP50:95. Additionally, a clear task difficulty hierarchy emerges: all detectors achieve AP50 > 0.8 on structural components (VAL, SLE) but struggle to achieve AP50 > 0.3 on damage categories (MTL, GWA), highlighting that metal loss detection remains the critical bottleneck.

C.1.2 Per-Category Analysis (Damages and Components).

Damage-Type Features (MTL, CRC, GWA, SWA). The damage categories present distinct detection challenges due to extreme scale variation and category imbalance.

Metal Loss (MTL): As the dominant category, MTL shows surprising detection difficulty. YOLOv5-l achieves the highest AP50 (**0.286**), outperforming transformer alternatives (RF-DETR: 0.246, RT-DETR: 0.202). This suggests that anchor-based detection remains superior for densely packed micro-defects. Notably, despite MTL’s high frequency, no model achieves AP50 > 0.30, indicating inherent challenges in detecting sparse, low-contrast pitting signals against noisy backgrounds.

Corrosion Cluster (CRC): YOLO26-m achieves the best AP50 (**0.149**), followed by YOLO26-x (0.139). Most models exhibit higher recall than precision, suggesting that the localization ability of CRC suffers from poorly-defined boundaries and confusion with densely packed MTL. Models appear to detect the general area of corrosion clusters effectively (high recall), but struggle to precisely delineate their spatial extent against scattered metal loss.

Weld Anomalies (GWA and SWA): F1-scores generally improve with increasing model complexity across the YOLOv5, YOLOv8 and YOLO26 series, with YOLO11 being a notable exception. Among the 12 categories, GWA presents the greatest detection challenge (maximum AP50 of merely **0.076**), as it occurs exclusively on girth welds that exhibit substantial signal variations within the heat-affected zone, thereby obscuring anomaly boundaries. This thermal interference creates unstable feature representations even when metal loss is present, rendering GWA particularly elusive for detectors relying on consistent visual patterns. SWA constitutes another challenging category, as its inclined linear patterns closely resemble those of MTL and the two frequently co-occur within the same spatial regions, further complicating differentiation and localization.

Component-Type Features (BND, SLE, BRN, TEE, CAS, VAL, ESP, FLA). Component detection reveals a scale-dependent performance gap: Large Continuous Components (SLE, VAL, BND): These full-circumference features achieve high AP50 across most models (SLE:**0.880**, VAL:**0.919**, BND:**0.587**), validating that modern detectors handle large structural elements reliably. However, RT-DETR completely fails in SLE (AP50: “-”), likely due to its decoder’s inability to model continuous vertical structures spanning the full circumferential boundary.

Moderate-size Components (BRN and TEE): These exhibit high inter-class confusion. RF-DETR achieves the highest BRN AP50 (**0.479**) and strong BRN and TEE recall (**0.644**, 0.895), but YOLO models (e.g., YOLO26-n) excel in TEE and BRN precision (0.739, 0.889). This discrepancy suggests that transformer architectures better capture global spatial priors, such as the azimuthal constraints of BRN and TEE (concentrated at 0, 3 and 9 o’clock positions) and their contextual association with station scenes, thereby successfully retrieving more objects despite local feature ambiguity. Conversely, CNN-based detectors excel at precise geometric localization: YOLO models more accurately delineate the spherical boundaries of TEE and the spindle-shaped contours of BRN through localized edge and texture cues, resulting in tighter bounding boxes and fewer false positives on ambiguous background regions.

Long-tailed Components (FLA, ESP, CAS): These rare tail categories (combined <0.1% of objects) expose the brittleness of current approaches. Several models achieve relatively high recall (**0.750**) in FLA, but the precision is low. This arises because FLA patterns are visually similar to partial VAL segments. During patch-based

Table 10: Model comparison on PipeMFL-240K sub-dataset (Confidence score=0.25, IoU=0.5) with different scales (scale=1: 53,375 Positive + 5,930 Negative samples).

Model	Dataset Scale	mAP50	mAP50:95	Precision (macro, micro)	Recall (macro, micro)	F1-score (macro, micro)
YOLOv8-m	1	0.450	0.288	0.448, 0.375	0.596, 0.356	0.490, 0.365
YOLOv8-m	1/2	0.404	0.250	0.384, 0.315	0.541, 0.414	0.435, 0.358
YOLOv8-m	1/4	0.417	0.224	0.376, 0.245	0.563, 0.404	0.428, 0.305
YOLOv8-m	1/8	0.290	0.168	0.348, 0.232	0.407, 0.355	0.351, 0.280
YOLOv8-m	1/16	0.169	0.119	0.229, 0.213	0.281, 0.361	0.194, 0.268
RF-DETR-Base	1	0.472	0.273	0.378, 0.151	0.650, 0.514	0.460, 0.233
RF-DETR-Base	1/2	0.447	0.263	0.327, 0.157	0.650, 0.493	0.416, 0.238
RF-DETR-Base	1/4	0.413	0.250	0.327, 0.136	0.633, 0.499	0.408, 0.214
RF-DETR-Base	1/8	0.346	0.194	0.266, 0.138	0.552, 0.460	0.332, 0.213
RF-DETR-Base	1/16	0.256	0.160	0.220, 0.137	0.433, 0.405	0.274, 0.205
YOLO26-m	1	0.442	0.263	0.585, 0.436	0.550, 0.291	0.536, 0.349
YOLO26-m	1/2	0.418	0.239	0.512, 0.389	0.540, 0.323	0.497, 0.353
YOLO26-m	1/4	0.370	0.222	0.418, 0.339	0.494, 0.350	0.428, 0.345
YOLO26-m	1/8	0.184	0.126	0.327, 0.354	0.248, 0.300	0.239, 0.324
YOLO26-m	1/16	0.100	0.044	0.170, 0.283	0.167, 0.292	0.145, 0.288

Table 11: Comparison of AP50 for each category in models with different dataset scales (scale=1: 53,375 Positive + 5,930 Negative samples). "-" indicates not detected.

Model	Scale	Damage				Component							Overall	
		MTL	CRC	GWA	SWA	BND	SLE	BRN	TEE	CAS	VAL	ESP	FLA	
YOLOv8-m	1	0.243	0.113	0.051	0.090	0.571	0.871	0.362	0.771	0.531	0.891	0.651	0.250	0.450
YOLOv8-m	1/2	0.262	0.100	0.056	0.100	0.553	0.856	0.360	0.579	0.483	0.851	0.400	0.250	0.404
YOLOv8-m	1/4	0.217	0.069	0.044	0.074	0.529	0.714	0.234	0.512	0.359	0.849	0.651	0.750	0.417
YOLOv8-m	1/8	0.188	0.010	0.036	0.067	0.286	0.694	0.257	0.255	0.224	0.785	0.174	0.500	0.290
YOLOv8-m	1/16	0.181	0.030	0.024	0.053	0.184	0.733	-	0.053	-	0.723	-	0.050	0.169
RF-DETR-Base	1	0.246	0.128	0.070	0.108	0.501	0.810	0.479	0.878	0.365	0.849	0.477	0.750	0.472
RF-DETR-Base	1/2	0.211	0.127	0.045	0.069	0.442	0.724	0.353	0.861	0.471	0.776	0.785	0.500	0.447
RF-DETR-Base	1/4	0.194	0.082	0.049	0.055	0.426	0.660	0.463	0.750	0.524	0.776	0.636	0.286	0.413
RF-DETR-Base	1/8	0.191	0.134	0.050	0.090	0.229	0.685	0.443	0.655	0.214	0.703	0.477	0.279	0.346
RF-DETR-Base	1/16	0.151	0.046	0.031	0.051	0.119	0.613	0.338	0.547	0.158	0.690	0.333	-	0.256
YOLO26-m	1	0.206	0.149	0.032	0.088	0.430	0.829	0.346	0.775	0.452	0.864	0.386	0.750	0.442
YOLO26-m	1/2	0.223	0.109	0.030	0.091	0.418	0.865	0.333	0.719	0.401	0.840	0.574	0.417	0.418
YOLO26-m	1/4	0.212	0.081	0.032	0.082	0.455	0.819	0.278	0.566	0.271	0.835	0.478	0.333	0.370
YOLO26-m	1/8	0.189	0.012	0.015	0.062	0.275	0.640	0.084	-	0.165	0.764	-	-	0.184
YOLO26-m	1/16	0.162	0.009	0.004	0.026	0.019	0.497	-	-	-	0.472	-	0.006	0.100

processing, VAL frequently extends beyond single windows due to their large size, producing incomplete observations that geometrically mimic FLA. Specifically, the blue rectangular base with a single vertical red line of FLA resembles truncated VAL segments that lack their complete symmetric elliptical patterns. This spatial truncation of VAL during windowing creates ambiguous local features that are easily misclassified as FLA, thus degrading detection precision for both categories. Models in the YOLO family maintain moderate performance on CAS and ESP, which indicates that YOLO architectures maintain representational capacity for tail categories even when training data follow a highly skewed distribution.

C.1.3 Visualization Comparison.

Fig. 11-Fig. 19 provide more qualitative visualization results. Fig. 11-Fig. 13 contain dense damage-type categories. Transformer-based models RF-DETR and RT-DETR, as well as RetinaNet detect much more metal losses, corresponding to their high recall values shown in Table 8, while the detection results are duplicated and located at the wrong region, leading to low precision, these models can detect more head-class objects, but false positives are also higher. In contrast, YOLO series has balanced ability to detect and locate, YOLOv8-l outperforms among all YOLO models on this case.

Fig. 14-Fig. 16 contain multiple types of component categories. YOLO-series and RF-DETR detect most of the components correctly,

Table 12: Comparison of Precision for each category in models with different dataset scales (scale=1: 53,375 Positive + 5,930 Negative samples). "-" indicates not detected.

Model	Scale	Damage				Component								Overall
		MTL	CRC	GWA	SWA	BND	SLE	BRN	TEE	CAS	VAL	ESP	FLA	
YOLOv8-m	1	0.401	0.111	0.339	0.269	0.451	0.639	0.609	0.689	0.329	0.789	0.500	0.250	0.448
YOLOv8-m	1/2	0.335	0.085	0.278	0.229	0.434	0.541	0.512	0.563	0.469	0.719	0.191	0.250	0.384
YOLOv8-m	1/4	0.268	0.064	0.195	0.148	0.428	0.565	0.484	0.647	0.324	0.767	0.429	0.188	0.376
YOLOv8-m	1/8	0.255	0.022	0.143	0.205	0.240	0.469	0.778	0.500	0.333	0.636	0.200	0.400	0.348
YOLOv8-m	1/16	0.241	0.029	0.128	0.156	0.137	0.485	-	1.000	-	0.476	-	0.100	0.241
RF-DETR-Base	1	0.167	0.108	0.173	0.064	0.326	0.398	0.518	0.694	0.333	0.697	0.313	0.750	0.378
RF-DETR-Base	1/2	0.172	0.086	0.146	0.074	0.299	0.345	0.362	0.783	0.227	0.657	0.667	0.105	0.327
RF-DETR-Base	1/4	0.153	0.057	0.127	0.064	0.250	0.537	0.406	0.667	0.295	0.731	0.539	0.098	0.327
RF-DETR-Base	1/8	0.148	0.063	0.140	0.084	0.196	0.275	0.294	0.519	0.444	0.667	0.304	0.054	0.266
RF-DETR-Base	1/16	0.152	0.060	0.129	0.067	0.201	0.400	0.348	0.600	0.139	0.210	0.333	-	0.220
YOLO26-m	1	0.454	0.156	0.411	0.396	0.457	0.781	0.677	0.861	0.750	0.697	0.385	0.750	0.585
YOLO26-m	1/2	0.408	0.100	0.355	0.372	0.432	0.776	0.613	0.775	0.619	0.677	0.353	0.667	0.512
YOLO26-m	1/4	0.359	0.076	0.256	0.300	0.437	0.520	0.500	0.800	0.500	0.667	0.313	0.286	0.418
YOLO26-m	1/8	0.364	0.055	0.336	0.329	0.382	0.525	0.667	-	0.714	0.556	-	-	0.327
YOLO26-m	1/16	0.299	0.043	0.165	0.163	0.261	0.756	-	-	-	0.333	-	0.022	0.170

Table 13: Comparison of Recall for each category in models with different dataset scales (scale=1: 53,375 Positive + 5,930 Negative samples). "-" indicates not detected.

Model	Scale	Damage				Component								Overall
		MTL	CRC	GWA	SWA	BND	SLE	BRN	TEE	CAS	VAL	ESP	FLA	
YOLOv8-m	1	0.390	0.401	0.112	0.221	0.880	0.900	0.508	0.820	0.640	1.000	0.778	0.500	0.596
YOLOv8-m	1/2	0.457	0.380	0.143	0.272	0.827	0.914	0.489	0.711	0.600	1.000	0.444	0.250	0.541
YOLOv8-m	1/4	0.443	0.392	0.149	0.281	0.782	0.897	0.333	0.579	0.480	1.000	0.667	0.750	0.563
YOLOv8-m	1/8	0.402	0.134	0.135	0.193	0.565	0.793	0.311	0.368	0.240	0.913	0.333	0.500	0.407
YOLOv8-m	1/16	0.417	0.209	0.105	0.191	0.437	0.845	-	0.053	-	0.870	-	0.250	0.281
RF-DETR-Base	1	0.553	0.390	0.236	0.446	0.852	0.879	0.644	0.895	0.600	1.000	0.556	0.750	0.650
RF-DETR-Base	1/2	0.534	0.427	0.232	0.387	0.797	0.845	0.556	0.947	0.680	1.000	0.889	0.500	0.650
RF-DETR-Base	1/4	0.535	0.450	0.247	0.425	0.776	0.879	0.622	0.842	0.720	0.826	0.778	0.500	0.633
RF-DETR-Base	1/8	0.503	0.418	0.174	0.408	0.573	0.793	0.556	0.737	0.320	0.870	0.778	0.500	0.552
RF-DETR-Base	1/16	0.451	0.310	0.139	0.331	0.406	0.793	0.533	0.632	0.360	0.913	0.333	-	0.433
YOLO26-m	1	0.322	0.368	0.059	0.169	0.748	0.862	0.467	0.816	0.480	1.000	0.556	0.750	0.550
YOLO26-m	1/2	0.363	0.340	0.067	0.186	0.701	0.897	0.422	0.816	0.520	1.000	0.667	0.500	0.540
YOLO26-m	1/4	0.394	0.303	0.089	0.193	0.723	0.879	0.378	0.632	0.320	0.957	0.557	0.500	0.494
YOLO26-m	1/8	0.354	0.094	0.036	0.139	0.466	0.724	0.089	-	0.200	0.870	-	-	0.248
YOLO26-m	1/16	0.361	0.061	0.019	0.119	0.044	0.586	-	-	-	0.565	-	0.250	0.167

especially VAL and SLE. They also identify one MTL object with an abnormal color pattern. Several models successfully figure out hard-to-detect BRNs, such as YOLOv5-m, YOLOv8-m, YOLO11-l, RT-DETR and RF-DETR.

Fig. 17-Fig. 19 contain tiny and low-response MTLs. Most models can detect these tiny damages, indicating that current models can handle small objects after being trained with large-scale data.

C.2 Data Scaling Study

Table 11- 14 show per-category metrics (AP50, Precision, Recall, F1-score) of models trained with different subsets. Key observations include: (i) The recall of head categories (predominantly damage

types) remains stable across different data scales, attributable to the sufficient presence of these frequent objects even in small subsets. Conversely, precision for head categories improves with larger training sets, indicating enhanced localization accuracy as more data become available. (ii) For medium-to-tail categories, both precision and recall generally increase with data scale, though the rarest categories (ESP, FLA) exhibit instability due to their extreme scarcity in the testing set. (iii) Overall performance improves consistently as the training subset approaches the full dataset, with YOLO26-m showing particularly pronounced sensitivity to data volume. (iv) Notably, all models exhibit substantial gains when scaling from 1/8 to 1/4 of the data, whereas the marginal improvement rate

Table 14: Comparison of F1-score for each category in models with different dataset scales (scale=1: 53,375 Positive + 5,930 Negative samples). "-" indicates not detected.

Model	Scale	Damage				Component								Overall
		MTL	CRC	GWA	SWA	BND	SLE	BRN	TEE	CAS	VAL	ESP	FLA	
YOLOv8-m	1	0.395	0.174	0.168	0.243	0.596	0.747	0.554	0.749	0.434	0.882	0.609	0.333	0.490
YOLOv8-m	1/2	0.387	0.139	0.188	0.249	0.569	0.679	0.500	0.628	0.526	0.836	0.267	0.250	0.358
YOLOv8-m	1/4	0.334	0.111	0.169	0.194	0.553	0.693	0.395	0.611	0.387	0.868	0.522	0.300	0.428
YOLOv8-m	1/8	0.312	0.038	0.139	0.199	0.337	0.590	0.444	0.424	0.279	0.750	0.250	0.444	0.351
YOLOv8-m	1/16	0.305	0.051	0.115	0.172	0.208	0.616	-	0.100	-	0.615	-	0.143	0.194
RF-DETR-Base	1	0.256	0.169	0.200	0.112	0.472	0.548	0.574	0.782	0.429	0.821	0.400	0.750	0.460
RF-DETR-Base	1/2	0.260	0.143	0.180	0.124	0.435	0.490	0.439	0.857	0.340	0.793	0.762	0.174	0.416
RF-DETR-Base	1/4	0.238	0.101	0.168	0.110	0.378	0.667	0.491	0.744	0.419	0.776	0.636	0.163	0.408
RF-DETR-Base	1/8	0.229	0.109	0.155	0.140	0.292	0.409	0.385	0.609	0.372	0.755	0.437	0.098	0.332
RF-DETR-Base	1/16	0.227	0.100	0.134	0.111	0.269	0.532	0.421	0.615	0.200	0.341	0.333	-	0.274
YOLO26-m	1	0.377	0.219	0.103	0.237	0.567	0.820	0.553	0.838	0.585	0.821	0.455	0.857	0.536
YOLO26-m	1/2	0.384	0.155	0.113	0.248	0.534	0.832	0.500	0.795	0.565	0.807	0.462	0.571	0.497
YOLO26-m	1/4	0.376	0.122	0.132	0.235	0.544	0.654	0.430	0.706	0.390	0.786	0.400	0.364	0.428
YOLO26-m	1/8	0.359	0.069	0.065	0.196	0.420	0.609	0.157	-	0.313	0.678	-	-	0.239
YOLO26-m	1/16	0.327	0.051	0.034	0.138	0.075	0.660	-	-	-	0.419	-	0.041	0.145

decreases at higher scales ($1/4 \rightarrow 1/2 \rightarrow 1$) because at these stages, the model has possessed an adequate detection performance.

D Broader Impact

This work introduces PipeMFL-240K, a large-scale, publicly available, carefully annotated dataset and benchmark for complex object detection in pipeline MFL imagery. By covering various damage types, structural components, inspection scenes and pipe configurations under real in-service conditions, this dataset provides a standardized foundation for advancing research on automated pipeline inspection and structural integrity assessment.

The authors do not anticipate any negative social impacts resulting from the release of this dataset. On the contrary, the expected impact is largely positive. PipeMFL-240K enables the development and rigorous evaluation of robust inspection algorithms that can better handle extreme category imbalance, scale variation and strong

structural context, which are common challenges in real-world industrial inspection scenarios. By reducing the reliance on manual inspection and expert-driven annotation, the proposed benchmark can facilitate more efficient and consistent condition monitoring of critical pipeline infrastructure.

In a broader industrial and societal context, this work has the potential to improve the safety and reliability of energy transportation systems by supporting earlier and more accurate detection of safety-critical defects. Such advances may help prevent pipeline failures, reduce environmental risks and lower maintenance costs. Furthermore, by providing an open and reproducible benchmark, this dataset promotes transparent comparison across methods and accelerates the translation of machine learning research into practical, trustworthy inspection systems, particularly in large-scale or resource-constrained operational environments.